1 **OMI/Aura Nitrogen Dioxide Standard Product Version 4.0 with Improved Surface**
2 **and Cloud Treatments**
3

5 Lok N. Lamsal [*,1,2], Nickolay A. Krotkov[2], Alexander Vasilkov[2,3], Sergey Marchenko[2,3],
6 Wenhan Qin[2,3], Eun-Su Yang[2,3], Zachary Fasnacht[2,3], Joanna Joiner[2], Sungyeon Choi[2,3], David
7 Haffner[2,3], William H. Swartz[4], Bradford Fisher[2,3], Eric Bucsela[5]
8
9 [1]University Space Research Association, Greenbelt, MD 20770, USA
10 [2]NASA Goddard Space Flight Center, Greenbelt, MD 20770, USA
11 [3]Science Systems and Applications, Lanham, MD 20706, USA
12 [4]Johns Hopkins University, Applied Physics Laboratory, Laurel, MD 20723, USA
13 [5]SRI International, Menlo Park, CA 94025, USA
14
15
16
17 [*]Corresponding author: Email: lok.lamsal@nasa.gov.

18   **Abstract**

19   We present a new and improved version (V4.0) of the NASA standard nitrogen dioxide (NO_2)

20   product from the Ozone Monitoring Instrument (OMI) on the Aura satellite. This version

21   incorporates the most salient improvements for OMI NO_2 products suggested by expert users and

22   enhances the NO_2 data quality in several ways through improvements to the air mass factors

23   (AMFs) used in the retrieval algorithm. The algorithm is based on geometry-dependent surface

24   Lambertian equivalent reflectivity (GLER) operational product that is available on an OMI pixel

25   basis. GLER is calculated using the vector linearized discrete ordinate radiative transfer

26   (VLIDORT) model, which uses as input high resolution bidirectional reflectance distribution

27   function (BRDF) information from NASA's Aqua Moderate Resolution Imaging

28   Spectroradiometer (MODIS) instruments over land and the wind-dependent Cox–Munk wave-

29   facet slope distribution over water, the latter with contribution from the water-leaving radiance.

30   The GLER combined with consistently retrieved oxygen dimer (O_2-O_2) absorption-based effective

31   cloud fraction (ECF) and optical centroid pressure (OCP) provide improved information to the

32   new NO_2 AMF calculations. The new AMFs increase the retrieved tropospheric NO_2 by up to 50%

33   in highly polluted areas; these differences arise from both cloud and surface BRDF effects as well

34   as biases between the new MODIS-based and previously used OMI-based climatological surface

35   reflectance data sets. We quantitatively evaluate the new NO_2 product using independent

36   observations from ground-based and airborne instruments. The new V4.0 data and relevant

37   explanatory documentation are publicly available from the NASA Goddard Earth Sciences Data

38   and Information Services Center (https://disc.gsfc.nasa.gov/datasets/OMNO2_V003/summary/),

39   and we encourage their use over previous versions of OMI NO_2 products.

Introduction

The Dutch/Finnish-built Ozone Monitoring Instrument (OMI) has been operating on board the NASA EOS-Aura spacecraft since July 2004 (Levelt et al., 2006, 2018). The primary objectives of OMI's mission are to continue the long-term record of total column ozone and to monitor other trace gases relevant to tropospheric pollution worldwide. Observations of sunlight backscattered from the Earth over a wide range of UV and visible wavelengths (~260-500 nm) made by OMI allow for the retrieval of various atmospheric trace gases, including nitrogen dioxide (NO_2). NO_2 is a critically important short-lived air pollutant originating from both anthropogenic and natural sources. It is the principal precursor to tropospheric ozone and a key agent for the formation of several toxic airborne substances such as nitric acid (HNO_3), nitrate aerosols, and peroxyacetyl nitrate. Satellite-based observations yield a global, self-consistent NO_2 data record that can complement field measurements.

During more than 16 years of operation, OMI has provided a unique, practically uninterrupted daily NO_2 data record that has been widely used for atmospheric research and applications, accentuating demands for accurate NO_2 data products. The power of OMI to track NO_2 pollution is demonstrated through observations of enhanced column amounts over polluted industrial areas (*e.g.*, Boersma et al., 2011; Lamsal et al., 2013; Krotkov et al., 2016; Kim et al., 2016; Cai et al., 2018; Montgomery and Halloway, 2018), weekly patterns with significant reduction on weekends following energy usage (*e.g.*, Ialongo et al., 2016), and seasonal patterns (e.g., van der A et al., 2008) that reflect changes in NO_x emissions and photochemistry (*e.g.*, Shah et al., 2019). Exploiting the close relationship between NO_x emissions and tropospheric NO_2 columns, OMI NO_2 data have been used to detect and quantify the strength and trends of NO_x emissions from power plants (Duncan et al., 2013; de Foy *et al.*, 2015; Liu et al., 2019), ships (*e.g.*, Vinken et al., 2014a), lightning (*e.g.*, Picketing et al., 2016), soil (*e.g.*, Vinken et al., 2014b), oil and gas production (e.g., Dix et al., 2020), forest fires (Schreier et al, 2014), and other area sources such as cities in the US (Lamsal *et al.,* 2015; Lu *et al.,* 2015; Kim et al., 2016), Europe (*e.g.*, Zhou et al., 2012; Castellanos et al., 2012; Vinken et al., 14a), Asia (Ghude et al., 2013; Goldberg et al., 2019a), and other world urban areas (Krotkov *et al.,* 2016; Duncan *et al.*, 2016; Montgomery and Halloway, 2018). OMI NO_2 observations have frequently seen used to evaluate chemical transport models (CTMs) (*e.g.*, Herron-Thrope et al., 2010; Han et al., 2011; Hudman et al., 2012; Pope et al., 2015; Rasool et al., 2016), to study atmospheric NO_x chemistry and lifetime (*e.g.*, Lamsal et

71 al., 2010; Beirle et al., 2011; Canty et al., 2015; Tang et al., 2015; Laughner and Cohen, 2019),

72 and to infer ground-level NO_2 concentrations (Lamsal et al., 2008; Gu et al., 2017), NO_2 dry

73 deposition (Nowlan et al., 2014, Geddes and Martin, 2017), and emissions of co-emitted gases

74 including carbon dioxide (CO_2) (Konovalov et al., 2016; Goldberg et al., 2019b, Liu et al., 2019).

75 Over the last decade, there have been considerable efforts to improve NO_2 data quality from OMI

76 and other satellite instruments (e.g., Boersma et al., 2018). A special emphasis has been placed on

77 improving auxiliary information (e.g., a priori NO_2 vertical profiles, surface reflectivity),

78 particularly with respect to spatial and temporal resolution. For instance, the global OMI NO_2

79 products are based on a priori NO_2 profiles from relatively coarse-resolution (>1.0°× 1.25°) global

80 CTM simulations (Boersma et al., 2011; Krotkov et al., 2017, Choi et al., 2020). Many regional

81 studies suggest a general low-bias in the global tropospheric NO_2 column products, particularly

82 over polluted areas, that can be partially mitigated by using a-priori information from high-

83 resolution CTM simulations (Russell et al., 2011, McLinden et al., 2014; Lin et al., 2014; 2015;

84 Goldberg et al., 2018; Choi et al., 2020). Current global NO_2 retrievals are based on a low-

85 resolution (0.5°× 0.5°) static climatology of surface Lambert-Equivalent Reflectivity (OMLER)

86 product (Kleipool et al., 2008), which is likely biased high due to insufficient cloud and aerosol

87 screening. This bias in surface reflectivity can lead to an underestimation of tropospheric NO_2

88 retrievals (Zhou et al., 2010; Lin et al., 2014; Vasilkov et al., 2017). In addition, the OMLER data

89 do not account for the significant day-to-day (orbital) variability in surface reflectance caused by

90 changes in sun-satellite geometry, a phenomenon often expressed by the bi-directional reflectance

91 distribution function (BRDF). Zhou et al. (2010) demonstrated the impact of both the spatial

92 resolution and the BRDF effect on OMI tropospheric NO_2 retrievals over Europe by using high-

93 resolution surface BRDF and albedo products from the Moderate Resolution Imaging

94 Spectroradiometer (MODIS). Taking advantage of the MODIS high resolution data, albeit

95 neglecting the BRDF and atmospheric effects, Russell et al (2011) and McLinden et al (2014)

96 created improved NO_2 products from the NASA Standard Product (Bucsela et al., 2013; Lamsal

97 et al., 2014) over the continental US and Canada, respectively. While these and subsequent studies

98 (e.g., Kuhlmann et al., 2015; Laughner et al., 2019) addressed the limitation of climatological LER

99 data on NO_2 retrievals, they did not account for the surface BRDF effect on the OMI cloud products

100 (cloud pressure/fraction), which are also inputs to the NO_2 algorithm. Applying the MODIS BRDF

101 data consistently to both the NO_2 and cloud retrievals demonstrably improves the quality of OMI

NO$_2$ retrievals over China (Lin et al., 2014, 2015, Liu et al., 2019). However, this approach is computationally expensive and is applicable to land surfaces only. Our previous work (Vasilkov et al., 2018) proposed an approach appropriate for satellite NO$_2$ data processing on a global scale (a) by using MODIS BRDF information consistently in the cloud and NO$_2$ retrievals; (b) for both land and water; and (c) in an efficient way. Here, we apply the approach globally for the first time in the standard NASA OMI NO$_2$ algorithm.

In this paper we describe various updates made in the version 4.0 (V4.0) NASA OMI NO$_2$ algorithm, discuss their impact on the retrievals of tropospheric and stratospheric NO$_2$ column amounts, and provide an initial quantitative assessment of NO$_2$ data quality. Section 2 describes the OMI NO$_2$ algorithm and various auxiliary data used by the algorithm. We present validation results in Section 3. Section 4 summarizes the conclusions of this study.

2 OMI and the NO$_2$ Standard Product

OMI is a ultraviolet-visible (UV-Vis) spectrometer on the polar-orbiting NASA Aura satellite (Levelt et al., 2006, 2018). Aura, launched on July 15, 2004, follows a sun-synchronous orbit with an equator crossing time near 13:45 local time. OMI employs two-dimensional CCD detectors and operates in a push-broom mode, registering spectral data over a 2600 km cross-track spatial swath. The broad swath enables global daily coverage within 14-15 orbits. In the OMI visible channel used for NO$_2$ retrievals, each swath, measured every two seconds, comprises 60 cross-track fields of view (FOVs) varying in size from ~13 km × 24 km near nadir to ~24 km × 160 km for the FOVs at the outermost edges of the swath. Each orbit consists of ~1650 swaths from terminator to terminator. OMI's full daily coverage has been affected by data loss due to an anomaly presumably caused by material on the spacecraft outside the instrument that results in reduced coverage to about half of its original swath as discussed in Section 2.4.

The OMI NO$_2$ Standard Product (OMNO2) algorithm provides retrievals of NO$_2$ column (total, tropospheric, and stratospheric) amounts by exploiting Level-1B calibrated radiance and irradiance data from the Vis channel (350-500 nm with 0.63 nm spectral resolution). The algorithm employs a multi-step procedure that consists of 1) a spectral fitting algorithm to calculate NO$_2$ slant column densities (SCDs) as discussed in Section 2.1; 2) determination of air mass factors (AMFs) to convert SCDs to vertical column densities (VCDs) as discussed in detail in Section 2.2; 3) a scheme to remove cross-track dependent artifacts or stripes; and 4) a stratosphere-troposphere separation scheme to derive tropospheric and stratospheric NO$_2$ VCDs. The AMF depends upon a

133 number of parameters including optical geometry (solar and viewing azimuth and zenith angles),
134 surface reflectivity, cloud pressure and fraction, and the shape of the NO_2 a priori vertical profile.

135 Since the first release of OMNO2 in 2006 (Bucsela et al., 2006; Celarier et al., 2008), there have
136 been significant conceptual and technical improvements in the retrieval of NO_2 from space-based
137 measurements. Prior versions developed a new scheme for separating stratospheric and
138 tropospheric components in version 2.1 (V2.1) (Bucsela et al., 2013, Lamsal et al., 2014) and a
139 new algorithm for improved NO_2 SCD retrievals in V3.0 (Marchenko et al., 2015, Krotkov et al.,
140 2017), and included improved cloud products (Veefkind et al., 2016) in V3.1 (Choi et al., 2020).
141 The current version, V4.0, further improves on the retrievals in a number of significant ways for
142 NO_2 AMF and VCD calculations. Figure 1 shows a schematic diagram of the retrieval algorithm,
143 and Table 1 summarizes the differences and similarities between previous (V3.1) and current (V4)
144 versions. Some of the approaches in the V4 algorithm are similar to those used in V3.1, but there
145 are several important changes as discussed in detail in Sections 2.1 and 2.2.

146 **2.1 NO_2 and O_2-O_2 spectral fitting**

147 **2.1.1 NO_2 spectral fitting algorithm**

148 The spectral fitting algorithm for the operational standard OMI NO_2 product is described in detail
149 in Marchenko et al. (2015). Briefly, the algorithm retrieves NO_2 slant column densities (SCDs) by
150 using a Differential Optical Absorption Spectroscopy (DOAS) approach (e.g., Platt and Stutz,
151 2006). In the DOAS approach, laboratory-measured spectra of NO_2 (Vandaele et al., 1998) and
152 glyoxal (Volkamer et al., 2005), HITRAN08-based water vapor spectra (Rothman et al., 2009),
153 and rotational Raman (RR; Ring effect) filling-in are sequentially fitted to the OMI-measured
154 reflectance spectrum in the 402-465 nm wavelength range. The slant column represents the
155 integrated abundance of NO_2 along the average photon path from the Sun, through the atmosphere,
156 to the satellite. The Ring spectra are calculated as a linear combination of the atmospheric (Joiner
157 et al. 1995) and the liquid-water (Vasilkov et al., 2002) RR spectra, convolved with the wavelength
158 and cross-track dependent OMI transfer function (Dirksen et al., 2006). The algorithm employs a
159 multi-step, iterative retrieval procedure for removal of the Ring and spectral under-sampling
160 (Chance, et al., 2005) patterns as well as a low-order polynomial smoothing prior to estimation of
161 SCDs for all interfering species. This is in contrast with the conventional DOAS approach that
162 treats the Ring effect as a pseudo-absorber and fits all absorbers simultaneously with the

163   polynomial functions. For accurate wavelength shifts (radiances vs. irradiances), the standard

164   product algorithm splits the entire fitting window into seven carefully selected, partially

165   overlapping micro-windows, iteratively evaluates the RR spectrum amplitudes, performs

166   wavelength adjustments for each segment, and then iteratively retrieves the NO_2, H_2O, and glyoxal

167   in the windows best suited for a particular trace-gas species.

168   The OMI NO_2 SCDs from the standard product were compared with improved SCD retrievals

169   from the Quality Assurance for Essential Climate Variables (QA4ECV, http://www.qa4ecv.eu/),

170   BIRA-IASB's (Royal Belgian Institute for Space Aeronomy) QDOAS software (http://uv-

171   vis.aeronomie.be/software/QDOAS/), and the latest KNMI retrievals (van Geffen et al., 2015) and

172   are shown to agree within 2% (Zara et al., 2018). The typical NO_2 SCD uncertainties amount to

173    $\sim 0.8 \times 10^{15}$ molec cm^{-2}, or 5-7% in high-SCD areas and 15-20% in low-SCD values (Marchenko et

174   al., 2015).

175   **2.1.2 O_2-O_2 spectral fitting algorithm**

176   The oxygen dimer (O_2-O_2) slant column fitting algorithm shares many features of the NO_2 fitting

177   algorithm and is described in detail in Vasilkov et al. (2018). It consists of a multi-step, iterative

178   retrieval approach with three carefully selected micro-windows sampling the flanks and the core

179   of the broad O_2-O_2 feature centered at 477 nm. The algorithm exploits OMI-measured reflectance

180   spectra in the 451-496 nm range to determine the wavelength shifts and RR amplitudes. The Ring

181   patterns are removed from the original OMI reflectances during the iterative adjustments for

182   differences in the wavelength registration of radiances and irradiances. The O_2-O_2 slant columns

183   are retrieved after removal of the NO_2 and H_2O absorptions estimated by the algorithm discussed

184   in the previous section, and of the ozone absorption using total ozone data from Veefkind et al.

185   (2006). After removal of the interfering signals, the 477 nm O_2-O_2 absorption profile is carefully

186   normalized to the adjacent O_2-O_2 absorption-free reflectance levels accounting for very different

187   wavelength dependencies of surface reflectances over various geographical sites (e.g., the open-

188   ocean and desert area), as described in Vasilkov et al. (2018). The normalized O_2-O_2 absorption

189   profiles are then iteratively fitted with the temperature-dependent cross-sections from Thalman

190   and Volkamer (2013) over the 463-488 nm range to derive O_2-O_2 SCDs. These are used to estimate

191   the cloud properties as discussed below in Section 2.2.2.

2.2 Improved air mass factor calculations

The AMF, which is defined as the ratio of SCD to VCD, is needed to calculate the retrieved NO_2 VCD. Details of the AMF and its calculation are given in Palmer et al. (2001). The AMF for each FOV is calculated by combining altitude (z)-dependent scattering weights (w) computed with a radiative transfer model and a local a priori vertical NO_2 profile shape (S), taken from a chemistry-transport model:

$$AMF = \int_{z_1}^{z_2} w(z)S(z)dz. \tag{1}$$

For the tropospheric AMF, the integral extends from the surface to the tropopause, whereas the integral from the tropopause to the top of the atmosphere provides the stratospheric AMF. The scattering weight at a given altitude describes the sensitivity of the backscattered radiation to the abundance of the absorber at that altitude. For an optically thin absorber like NO_2, scattering weights are a function of atmospheric scattering and are considered to be independent of the species' vertical distribution (Palmer et al., 2001). Factors affecting scattering weights include wavelength, optical geometry (solar and viewing azimuth and zenith angles), surface reflectivity, and cloud pressure and fraction. The wavelength dependence of scattering weights is accounted for by creating an average of scattering weights derived from the values at multiple wavelengths within the NO_2 spectral fitting window. To compensate for the effect of the assumed constant NO_2 temperature (220 K) in the NO_2 SCD retrievals, the scattering weights are corrected for the atmospheric temperature effect using local climatological monthly temperature profiles as discussed in Bucsela et al. (2013). These profiles are based on the meteorological field from the Modern-Era Retrospective Analysis for Research and Applications (MERRA-2) (Gelaro et al., 2017).

The a priori NO_2 profile shapes are computed from a monthly mean climatology of vertical NO_2 profiles constructed from the Global Modeling Initiative (GMI) CTM simulation (Douglass et al. 2004, Strahan et al., 2007, Strode et al., 2015) driven by MERRA-2 meteorology. The spatial resolution of the model is 1.25° in longitude and 1.0° in latitude, and the atmosphere is divided into 72 pressure levels extending from the surface to 0.01 hPa. The model output is sampled between 13:00 - 14:00, local time, consistent with the OMI overpass time. The use of monthly NO_2 profiles helps capture the seasonal variation in the NO_2 vertical distribution (Lamsal et al., 2010). The simulation is based on yearly varying NO_x emissions, as discussed in Strode et al., (2015); this is necessary to account for the effect of rapidly changing NO_x emissions (e.g., Tong

223 et al., 2015; Duncan et al., 2016; Miyazaki et al., 2017) on local NO$_2$ profile shapes (Lamsal et al.,

224 2015; Krotkov et al., 2017).

225 For each FOV, AMFs are computed for clear (AMF_{clr}) and cloudy (AMF_{cld}) conditions. The AMF

226 of a partially cloudy scene is calculated by assuming the independent pixel approximation:

227 $$AMF = (1 - f_r) \times AMF_{clr} + f_r \times AMF_{cld}, \tag{2}$$

228 where f_r is the cloud radiance fraction (CRF), defined as the fraction of the measured radiation

229 that comes from clouds and scattering aerosols, and is computed at 440 nm from the retrieved

230 effective cloud fraction (ECF), f_c using Equation 8 (see below). AMF_{clr} is calculated for the

231 ground reflectivity of R_s and at terrain pressure P_s, whereas AMF_{cld} is calculated assuming a

232 Lambertian surface of reflectivity 0.8 at the retrieved cloud pressure. Below we provide a detailed

233 discussion of each of these input parameters that are incorporated in the OMNO2 V4.0 algorithm.

234 **2.2.1 New surface reflectivity product for NO$_2$ and cloud retrievals**

235 Surface reflectivity is an important input parameter for UV/Vis satellite retrievals of trace gases

236 and cloud information. The surface reflectance over both ocean and land depend upon viewing and

237 illumination geometry and can be accurately described by the bidirectional reflectance distribution

238 function (BRDF). This effect is, however, neglected by most currently available trace gas and

239 cloud algorithms which use a climatological Lambert-equivalent reflectivity (LER) for the surface.

240 To account for surface BRDF effects in the NO$_2$ and cloud retrievals, here we use the geometry-

241 dependent surface LER (GLER) product derived using the Moderate Resolution Imaging

242 Spectroradiometer (MODIS) BRDF data and the Vector Linearized Discrete Ordinate Radiative

243 Transfer (VLIDORT) calculation (Vasilkov et al., 2017; Qin et al., 2019; Fasnacht et al., 2019).

244 The GLER allows for a computationally efficient approach that does not require major changes to

245 the existing trace gas and cloud algorithms.

246 We derive GLER by inverting the top-of-atmosphere (TOA) radiance (*I*) of a Rayleigh atmosphere

247 over a non-Lambertian surface for each specific FOV and Sun-satellite geometry within the

248 Lambertian framework, i.e.,

249 $$I = I_0 + GLER \times T/(1 - GLER \times S_b), \tag{3}$$

250 where I_0 is the TOA radiance calculated for a black surface, T is the total (direct + diffuse) solar

251 irradiance reaching the surface converted to the ideal Lambertian-reflected radiance (by dividing

252 by π steradians) and then multiplied by the transmittance of the reflected radiation between the

253 surface and TOA in the direction of a satellite instrument, and S_b is the diffuse flux reflectivity of

254 the atmosphere for the case of its isotropic illumination from below (Dave, 1978). The value of I_0,

255 T, and S_b are pre-computed with VLIDORT and stored in a look-up table. The GLER values are

256 calculated at wavelengths relevant for both NO_2 (440 nm) and cloud (466 nm) retrievals.

257 Over land, the BRDF is calculated using the Ross-Thick Li-Sparse kernel model (Lucht et al.,

258 2000) in VLIDORT (Spurr, 2006):

259 $$BRDF = a_{iso} + a_{vol}k_{vol} + a_{geo}k_{vol}, \tag{4}$$

260 where the coefficients, a_{iso}, a_{vol}, and a_{geo} come from the Moderate Resolution Imaging

261 Spectroradiometer (MODIS) Collection 5 gap-filled, seasonal snow-free BRDF product

262 MCD43GF (Schaaf et al., 2002, 2011) for band 3 (459-479 nm) available at 30 arc-second spatial

263 resolution and 8-day temporal resolution. The term a_{iso} is the isotropic contribution describing the

264 Lambertian part of light reflection from the surface, the volumetric kernel (k_{vol}) describes light

265 reflection from a dense leaf canopy, and the geometric kernel (k_{geo}) describes light reflection from

266 a sparse ensemble of surface objects casting shadows on the background assumed to be

267 Lambertian. The kernels are the only angle-dependent functions, the expressions of which are

268 given in Lucht et al. (2000). The band 3 BRDF coefficients spatially averaged over an actual

269 satellite FOV are used to calculate TOA radiance and GLER at 466 nm. To calculate GLER at 440

270 nm, we apply a scaling method using the ratio of OMI-derived lambert equivalent reflectivity

271 (LER) data at 440 nm and 466 nm:

272 $$GLER_{440} = GLER_{466} \times f_s. \tag{5}$$

273 The value of $f_s = \frac{LER_{440}}{LER_{466}}$ is taken from the gridded monthly LER ratio data at $1° \times 1°$ or coarser

274 resolution. The LER is determined from OMI TOA radiance measurements as discussed in

275 Vasilkov et al. (2017, 2018). We use clear-sky (effective cloud fraction <0.02) and aerosol free

276 (OMI UV Aerosol Index (Torres et al., 2007) <0.5) OMI LER data to create the monthly gridded

277 data. The cloud and aerosol screening is necessary because the spectral dependence of surface

278 features differ from that of clouds and aerosols.

279 Over water, the surface reflectance is calculated at the two wavelengths, 440 nm and 466 nm, using

280 VLIDORT. To calculate TOA radiance, we include light specularly reflected from a rough water

281 surface as well as diffuse light backscattered by water bulk. We also account for contributions

282 from oceanic foam that can be significant for high wind speeds. Reflection from the water surface

283   is described by the Cox–Munk slope distribution function, which depends on both the wind speed

284   and the wind direction (Cox and Munk, 1954). Polarization at the ocean surface is accounted for

285   by using a full Fresnel reflection matrix as suggested by Mishchenko and Travis (1997).

286   We use wind speed data from a pair of satellite microwave imagers that include the Advanced

287   Microwave Scanning Radiometer - Earth Observing System (AMSR-E) instrument onboard the

288   NASA Aqua satellite (Wentz and Meissner, 2004) for 2004-2011 and the Special Microwave

289   Imager/Sounder (SSMIS) onboard the Air Force Defense Meteorological Satellite Program

290   (DMSP) Satellite F16 (Wentz et al., 2012) afterwards. Wind direction data are taken from the

291   Global Modeling Assimilation Office (GMAO) Goddard Earth Observing System Model Forward

292   Processing for Instrument Teams (GEOS-5 FP-IT) near real time assimilation.

293   Diffuse light from the ocean is described by a Case 1 water model with a single input parameter

294   of chlorophyll concentration (Morel, 1988) taken from the monthly Aqua/MODIS data. The

295   common Case 1 water model developed for the Vis (Morel, 1988) was extended to the UV using

296   data from Vasilkov et al. (2002, 2005). To calculate water-leaving radiance, we require the

297   downwelling irradiance at the surface (i.e., atmospheric transmittance). Since the transmittance

298   and the water-leaving contribution are coupled, we develop a simple coupling scheme in

299   VLIDORT that ensures the value of water-leaving radiance used as an input at the ocean surface

300   will correspond to the correct value of the downwelling flux reaching the surface interface

301   (Fasnacht et al., 2019).

302   For OMI ground pixels covering land and water surfaces, the TOA radiance (I) is calculated as an

303   average of radiance for land (I_L) and water (I_w) weighted by the pixel land fraction (f):

304    $I = fI_L + (1 - f)I_w.$ (6)

305   The value of f is determined by converting various surface categories in the MODIS data (note

306   that these are of much higher spatial resolution than the OMI data) into a binary land-water mask

307   (e.g., treating all shorelines and ephemeral water as the land category and classifying all other

308   water sub-categories simply as water). The areal fraction of land (or water) for each OMI pixel is

309   then computed as the statistics of the binary categories.

310   Figure 2 shows an example of changes in surface reflectivity used in the previous (V3.1) and the

311   current (V4.0) version of the OMI NO$_2$ algorithm. The GLER data computed for OMI observations

312   as discussed above for March 20, 2005 differ considerably from the OMI-derived climatological

313   monthly LER data (Kleipool et al., 2008) for March. As shown in Figures 2 and 3(a), the GLERs

314   are generally lower than climatological LERs data except at swath edges with large viewing angles

315   and over areas affected by sunglint that correspond to higher values of GLER. Changes over the

316   sunglint areas are rather large, reaching up to 0.3. The climatological LER data derived by

317   analyzing histograms of five years of OMI-based LER data likely overestimate the actual surface

318   reflectivity due to residual cloud and aerosol contamination and underestimate over sunglint areas

319   as the procedure ignores sun glint affected observations. In contrast, the GLER data over land are

320   based on atmospherically corrected radiances from high-resolution MODIS observations,

321   minimizing the impact of both cloud and aerosols.

322   2.2.2 Improved cloud products retrieval

323   We develop a new algorithm that provides cloud parameters, namely cloud radiance fraction

324   (CRF) and cloud optical centroid pressure (OCP), and use them in the OMNO2 algorithm. Similar

325   to the standard OMCLDO2 algorithm (Veefkind et al, 2016), our cloud algorithm exploits the O_2-

326   O_2 absorption to retrieve O_2-O_2 SCD as discussed in Section 2.1.2, but derives the two cloud

327   parameters using the GLER and other ancillary data that are used in the NO_2 algorithm,

328   maintaining inter-algorithm consistency. The OMCLDO2 algorithm retrieves these parameters

329   using the climatological LER data from Kleipool et al. (2008). In the following, our new cloud

330   product is referred to as OMCDO2N.

331   The derivation of CRF and OCP is based on a simple cloud model called the mixed Lambertian-

332   equivalent reflectivity (MLER) model (Joiner and Vasilkov, 2006; Veefkind et al., 2016). The

333   MLER model treats cloud and ground as horizontally homogeneous, opaque Lambertian surfaces

334   and mixes them using the independent pixel approximation (IPA). According to the IPA, the

335   measured TOA radiance, I_m, is a sum of the clear-sky (I_g) and overcast (I_c) subpixel TOA

336   radiances that are weighted with an effective cloud fraction (ECF), f_c (e.g., Stammes et al., 2008):

337      $$I_m = I_g(1 - f_c) + I_c f_c. \qquad\qquad (7)$$

338   We choose the wavelength of 466 nm that is not substantially affected by rotational Raman

339   scattering (RRS) or atmospheric absorption to derive f_c. The parameters I_g and I_c are a function

340   of the ground and cloud LERs, respectively, and are calculated using VLIDORT (Spurr, 2006) and

341   obtained with an interpolated look up table. We use GLER discussed above for ground reflectivity

342 and a uniform cloud reflectivity of 0.8 (Koelemeijer et al., 2001; Stammes et al., 2008). The value

343 of f_c is calculated by inverting Equation (7). Note that aerosols are implicitly accounted for in the

344 determination of f_c, as they are treated (like clouds) as particulate scatters. CRF (f_r) defines the

345 fraction of TOA radiance reflected by cloud:

346 $$f_r = f_c \times \frac{I_c}{I_m}. \tag{8}$$

347 We use pre-computed look-up tables of the TOA radiances generated using VLIDORT. Due to its

348 wavelength dependence, we calculate CRF at 466 nm for OCP at 440 nm for NO_2 retrievals.

349 The MLER model compensates for photon transport within a cloud by placing the Lambertian

350 surface somewhere in the middle of the cloud instead of at the top (Vasilkov et al., 2008). The

351 pressure of this surface corresponds to OCP, which can be modeled as a reflectance-averaged

352 pressure level reached by backscattered photons (Joiner et al., 2012). We retrieve cloud OCP from

353 the O_2-O_2 SCD discussed above (Section 2.1.2). The cloud OCP, P_c, is estimated by inversion

354 using the MLER method to compute the appropriate O_2-O_2 AMFs:

355 $$SCD = AMF_g \times VCD_g \times (1 - f_r) + AMF_c \times VCD_c \times f_r, \tag{9}$$

356 where VCD (= SCD/AMF) is the vertical column density of O_2-O_2 over ground (VCD_g) and cloud

357 (VCD_c). The clear-sky (AMF_g) and overcast or cloudy (AMF_c) subpixel AMFs are calculated at

358 477 nm with ground (GLER) and cloud (0.8) reflectivity, respectively. Look-up tables for the

359 AMFs were generated using VLIDORT. Temperature profiles needed for estimation of VCD and

360 AMF are taken from the GEOS-5 global data assimilation system (Rienecker et al., 2011).

361 In addition to OCP, we retrieve the so-called scene pressure. The scene pressure is derived from

362 Eq. (9) assuming that $f_r = 1$ and cloud reflectivity = scene LER. The scene LER is determined

363 from the measured TOA radiance using the equation (Eq. 3) that defines TOA radiance in the

364 Rayleigh atmosphere over a Lambertian surface. In the absence of clouds, aerosols, and any major

365 gas absorptions, the scene pressure should be equal to the surface pressure. The scene pressure is

366 therefore an important diagnostic tool for evaluation of the performance of cloud pressure

367 algorithms.

368 Figure 4 shows an example of cloud products retrieved with our algorithm compared with those

369 retrieved from the standard OMCLDO2 algorithm (Veefkind et al., 2016). The retrieved OCP and

370 CRF from the two algorithms exhibit broadly consistent spatial patterns in both cloud altitude and

371 amount. The values of OCP generally range from 370 hPa to 1001 hPa in OMCDO2N versus 150

372 hPa to 1011 hPa in OMCLDO2N. For both products, CRF varies from 0 for clear-sky to 1 for

373 overcast conditions. A systematic difference is evident with generally higher values in OMCDO2N

374 for OCP by 147 hPa and CRF by 0.01 as compared to OMCLDO2. For OCP, there is a general

375 pattern in difference with OMCDO2N OCP higher for low-altitude clouds (>700 hPa) and lower

376 values for high-altitude clouds (<300 hPa) (Figure 3(c)). The largest OCP differences occur for

377 cases where cloud pressures in OMCLDO2 are clipped to 150 hPa. For CRF, larger differences

378 occur for partially cloudy scenes with higher CRF values in OMCDO2N by 0-0.1 for both land

379 and water surfaces (Figure 3(b)). Exceptions are over sun-glint areas, where CRF in OMCDO2N

380 is lower by 0-0.3 with the mean difference of 0.13.

381 **2.2.3 Treatment over snow and ice surfaces**

382 Over ice and snow surfaces, identified by the Near-real-time Ice and Snow Extent (NISE) flags

383 (Nolin et al., 2005) in the OMI Level 1b data, the following treatments are made for surface

384 reflectivity. In case of permanent ice and snow surfaces, the MCD43GF product provides BRDF

385 parameters, allowing us to calculate GLER. Over seasonal snow area usually with data gaps in

386 MCD43GF, we calculate OMI-derived LER but capped by a constant snow albedo of 0.6 following

387 Boersma et al. (2011). In rare cases of pixels not flagged by NISE and gaps in MODIS data, we

388 use OMI LER climatology (Kleipool et al., 2008), regardless whether the surface is either snow/ice

389 covered but missed by NISE or snow/ice free.

390 The OMI-derived scene reflectivity and scene pressure are used for NO_2 and cloud retrievals over

391 seasonal snow covered areas. If the NISE flags are set as true, the following assumptions are made

392 in our CRF, OCP, and NO_2 retrievals. Over bright surfaces (scene reflectivity > 0.2), we consider

393 the scenes as snow or cloud covered and assign the scene pressure to OCP. In addition, if a

394 difference between the surface pressure and scene pressure is smaller than 100 hPa, the scene is

395 considered to be either cloud free or covered by optically thin clouds following the cloud over

396 snow classification by Vasilkov et al. (2010), and CRF for the pixel is set to zero. If the difference

397 between the surface pressure and scene pressure exceeds 100 hPa, the scene is considered to be

398 overcast by optically thick (shielding) clouds (Vasilkov et al., 2010), and CRF for the pixel is set

399 to one. To avoid a possible NISE misclassification (Cooper et al., 2018) for low-reflectivity scenes

400 (scene reflectivity < 0.2), we consider such scenes as being snow/ice-free and calculate CRF, OCP,

401 and NO₂ AMF using the standard procedure with GLER for those scenes.

2.2.4 Improved terrain height/pressure calculation

403 Terrain pressure is a critical parameter to the AMF in NO₂ and cloud algorithms as well as to the

404 total optical depth of the Rayleigh atmosphere in the GLER algorithm. Prior studies have shown

405 that errors in terrain pressure can introduce over 20% errors in retrieved NO₂ VCD, especially in

406 areas of complex terrain (Zhou et al, 2010; Russell et al., 2011).

407 Here, we use a 2-arc minute Global Relief Model of global land-water surface data (ETOPOv2,

408 National Geophysical Data Center, 2006) to derive terrain height for each individual OMI ground

409 pixel. We derive the pixel-average terrain height by collocating and averaging the high resolution

410 data as discussed in Qin et al. (2019). The corresponding terrain pressure for each OMI pixel (P_s)

411 is calculated from the terrain pressure-height relationship established based on MERRA-2 monthly

412 terrain pressure (P_{s_GMI}) at a spatial resolution of 1° latitude × 1.25° longitude used in the GMI

413 model discussed above:

$$P_s = P_{s\_GMI}e^{-\left(\frac{\Delta z}{H}\right)}, \tag{10}$$

415 where Δz ($= z - z_{GMI}$) represents the difference between the average terrain height for an OMI

416 pixel (z) and the terrain height at GMI resolution (z_{GMI}). The parameter, $H = \frac{kT}{Mg}$, represents the

417 scale height, where k is the Boltzmann constant, T is the temperature at the surface, M is the mean

418 molecular weight of air, and g is the acceleration due to gravity.

2.3 Impact of the changes on AMF

420 Figure 5 shows an example of how changes in each individual input parameter affect tropospheric

421 AMFs which, in turn, translate inversely to tropospheric NO₂ column retrievals. Replacing

422 climatological LER from OMLER with daily GLER data affects scattering weight profiles in the

423 lower troposphere, resulting in lower values of tropospheric AMF almost everywhere, except over

424 sun glint areas, where the use of GLER enhances scattering weights and tropospheric AMF (Figure

425 5(a)). The changes in tropospheric AMF with GLER usually range from -50% to 25%,

426 occasionally reaching up to -100%. The effect is small (-6% to 1%) for overcast scenes (CRF>0.9),

427   and increases (-28% to 17%) over clear and partially cloudy scenes (CRF<0.5), for unpolluted

428   regions, and surges (-62% to 3%) over polluted areas (>5×10^{15} molec. cm^{-2}). Figure 6(a) shows

429   GLER-driven changes in clear-sky (CRF<0.5) tropospheric AMF for different surface and scene

430   types, separated by tropospheric NO$_2$ column amounts. For 80% of cases over land, 97% over

431   water outside of sunglint areas, and 98% over sunglint areas, tropospheric NO$_2$ columns are <

432   1.5×10^{15} molec. cm^{-2} and the average GLER-driven differences are small at –6.6±17.3%, -

433   3.8±7.1%, and 4.0±12.9%, respectively. The differences increase gradually with column amount

434   over NO$_x$ source regions (e.g., cities and highly polluted coastal areas) with binned (of size 1×10^{15}

435   molec. cm^{-2}) average differences ranging from -10±20.1% to -30±19.7%. Over snow and ice

436   surfaces, changes are rather large, reaching up to a factor of two. The impact of change in the

437   surface reflection data on stratospheric AMFs is negligible (<2%).

438   Figures 5(b) and 6(b) show how changes in the cloud parameters (CRF and OCP) affect

439   tropospheric AMF. Replacing OMCLDO2-based cloud parameters with those from OMCDO2N

440   changes scattering weight profiles in a complicated way. Higher values of OCP in OMCDO2N

441   will include additional portions of scattering weights between the OMCDO2N- and OMCLDO2-

442   based OCPs, especially in the lower troposphere, thereby reducing the tropospheric AMF. On the

443   other hand, the higher CRF values lead to an increased contribution of the cloudy AMF in the

444   calculation of tropospheric AMF, thereby increasing its value. Their combination causes a wide

445   range of scenarios as well as large variation in the AMF effect. Overall, the change in cloud

446   parameters causes enhancement of tropospheric AMFs for partially cloudy and overcast scenes

447   and reduction for clear-sky scenes, especially over polluted areas. The AMF differences are

448   generally large for low AMF values that are driven by enhanced differences in either OCP, CRF,

449   or both as discussed in Vasilkov et al (2017). The changes in tropospheric AMF with the

450   OMCDO2N-based cloud parameters usually range from -17% to 28% with a larger variation over

451   land (-34% to 40%) as compared to water (-12% to 25%), and for low (<1) AMF (-47% to 41%)

452   as compared to high (>3) AMF (-4% to 18%). The largest changes in AMF (-96% to 62%) occur

453   over snow and ice surfaces that result from the difference in the treatment of snow and ice for

454   cloud and NO$_2$ retrievals as discussed in Section 2.2.3. For clear-sky and partially cloudy scenes

455   with CRF < 0.5, the effect of the changes in cloud parameters differs between land and water

456   surfaces as well as sunglint and non-sunglint geometries and becomes more pronounced over

457 polluted land and coastal areas (Figure 6b). As in the case of surface reflectivity, the impact of the

458 change in cloud parameters on stratospheric AMF is <1%.

459 Figure 5c presents an example of changes in tropospheric AMF differences between the previous

460 approach of using terrain pressure at OMI pixel centers and the pixel average terrain pressure

461 implemented in the current version (V4.0). In general, the AMF changes driven by the changes in

462 terrain pressure are within ±1% over ocean and ±3% over land, although at times they can reach

463 up to 30%, especially for observations over complex terrain such as mountainous regions (Figure

464 5c inset).

465 Figures 5d and 6c show the AMF differences arising from the combined effect of changes in all

466 parameters discussed above. The effect arising from the replacement of the climatological OMLER

467 with GLER is partially compensated by the effect arising from the change in cloud parameters in

468 places where the two parameters exhibit opposite trend. Exceptions are over polluted land and

469 coastal areas, the GLER effect on AMF is augmented by the cloud effect. The average AMF

470 changes arising from all parameters (2%) are lower than the changes arising from either GLER (-

471 2.3%) or cloud parameters (4.1%), although the combined effect leads to a wider range of variation

472 in AMF changes (-100% to 57%) as compared to the effect from individual parameters. The

473 changes arising from all parameters are somewhat smaller (-21% to 34%) for overcast scenes

474 (CRF>0.9) as compared to (-47% to 29%) over clear and partially cloudy scenes (CRF<0.5), and

475 are substantial (-137% to 30%) over highly polluted areas (>5×10^{15} molec. cm^{-2}) and over snow/ice

476 surfaces (-126% to 99%). Differences in the AMF effect are evident among land, water, and

477 sunglint areas (Figure 6c). The impact of the changes is below 1% for the stratospheric AMF.

478 **2.4 Row anomaly and removal of stripes**

479 The retrieved NO$_2$ SCDs have persistent relative biases in the 60 cross-track FOVs and show a

480 pattern of stripes running along each orbital track. This instrumental artifact is corrected using the

481 "de-striping" procedure described in detail in Bucsela et al (2013). Briefly, the de-striping

482 algorithm estimates the mean cross-track biases using measurements obtained at latitudes between

483 30S and 5N and from orbits within 2 orbits of target orbit. These correction values, one for each

484 cross-track position, are then subtracted from the retrieved SCDs to derive the de-striped SCD

485 field.

486   Starting June 25, 2007 and presumably even earlier, OMI experienced a more severe form of

487   anomaly that affects the quality of radiance data in certain rows at all wavelengths (Dobber et al.,

488   2008; Schenkeveld et al., 2017). This effect, called the "row anomaly" (RA), has developed and

489   changed over time. Currently, the RA has affected approximately half of the OMI's FOVs,

490   resulting in OMI's global coverage now in two days instead of one before the onset of the RA.

491   The quality of radiance data for the RA-affected FOVs is sufficiently poor as to prevent reliable

492   NO$_2$ retrievals. Therefore, we abandon retrieval calculations for all measurements that are flagged

493   by the RA-detection algorithm used in the Level-1 processing. We found that this RA-detection

494   algorithm may not be sufficiently sensitive to the relatively small (but important for our purposes)

495   RA changes. Figure 7 shows an example of anomalous rows not flagged by the RA-detection

496   algorithm but observed in the NO$_2$ retrievals. Shown are time series of average NO$_2$ SCDs

497   normalized by geometric AMFs over the Pacific Ocean for the RA-unaffected row of 20 (0-based)

498   compared with three rows that show significant degradation in the quality of SCD retrievals. These

499   particular rows are in the immediate proximity to the main RA area, thus showing the gradual RA

500   evolution: at the present epoch the RA slowly shifts towards the high-numbered rows – note the

501   sequential timing of the big drops in the retrievals in the rows 44-46. While the data from the three

502   rows start deviating from row 20 beginning from summer 2016, the data quality degrades further

503   for rows 44, 45, and 46 from September of 2017, 2018, and 2019, respectively, to the extent that

504   they cannot be sufficiently corrected by the de-striping algorithm. In such cases, we implement

505   additional RA-flagging for those rows that start showing anomalous behavior, and exclude those

506   data from Level-2 and higher level NO$_2$ products.

507   **2.5 Calculation of stratospheric and tropospheric NO$_2$ columns**

508   We use an observation-based stratosphere-troposphere separation scheme to estimate the

509   stratospheric NO$_2$ field as discussed in detail in Bucsela et al. (2013), and the algorithm remains

510   unchanged in the current version. Briefly, the stratospheric field for an orbit is computed by

511   creating a gridded global field of initial stratospheric NO$_2$ VCD estimates (V_{init}) with data

512   assembled from within ±7 orbits of the target orbit:

513    $$V_{init} = \frac{S_{strat}}{AMF_{strat}} = \frac{S - S_{trop\_ap}}{AMF_{strat}}. \qquad (11)$$

514   Here S_{strat} and AMF_{strat} represent stratospheric SCD and AMF, respectively. An a priori

515   estimates of the tropospheric contribution (S_{trop_ap}) are subtracted from the measured, de-striped

516   SCDs (S), and grid cells where this contribution exceeds 0.3×10^{15} molecules cm^{-2} are masked.

517   This masking ensures that the model contribution to the retrieval is minimal, especially in the

518   polluted areas. The residual field of the initial stratospheric VCDs measured outside the masked

519   regions mainly over unpolluted or cloudy areas is smoothed by a boxcar average and a 2-

520   dimensional interpolation, yielding an estimate for stratospheric NO$_2$ VCD (V_{strat}) for an

521   individual ground pixel.

522   The estimation of the stratospheric NO$_2$ VCD allows for the computation of the tropospheric NO$_2$

523   VCD (V_{trop}) from the de-striped NO$_2$ SCD (S) and the tropospheric AMF (AMF_{trop}):

524   $$V_{trop} = \frac{S_{trop}}{AMF_{trop}} = \frac{S - S_{strat}}{AMF_{trop}}, \hspace{3cm} (12)$$

525   where stratospheric NO$_2$ SCD (S_{strat}) is calculated from stratospheric AMF (AMF_{strat}) and V_{strat}

526   computed in the previous step.

527   With the updates in surface and cloud treatments as discussed in Section 2.2, the current version

528   has made significant improvements particularly in tropospheric AMFs and consequently in VCD

529   estimates. Further improvement to the retrievals is possible by enhancing the quality of a priori

530   NO$_2$ profiles through improvements in model resolution, emissions, and chemistry, which remain

531   unchanged in the current version. If improved a priori NO$_2$ profiles become available, one can first

532   use Eq. 1 to readily re-calculate AMF_{trop} by combining them with scattering weights ($w(z)$)

533   archived in the data files and then use Eq. 12 together with other supplied parameters to re-

534   calculate V_{trop}. The same approach can be applied to remove the effect of a priori profiles used in

535   retrievals altogether, while comparing NO$_2$ columns from a model simulation with retrievals

536   (Eskes and Boersma, 2003; Lamsal et al., 2014).

537   Figure 8 shows a comparison of tropospheric and stratospheric NO$_2$ columns retrieved from V3.1

538   and V4.0 algorithms for 20 March, 2005. As expected, the updates implemented in V4.0 yield

539   higher (~10–40%) tropospheric NO$_2$ columns in polluted areas, with less-pronounced (±10%)

540   differences in background and low-column areas. These results are consistent with the observed

541   differences in the tropospheric AMF as discussed above in Section 2.2.4 as well as with other

542   previous regional studies over land surfaces (Zhou et al, 2010; McLinden et al, 2014; Lin et al.,

543   2014, 2015; Laughner et al., 2019; Liu et al., 2019) that implemented one or more of the changes

544   applied in V4.0. In contrast to changes in tropospheric NO$_2$ retrievals, changes in stratospheric

545   NO$_2$ estimates range between -3.6$\times 10^{14}$ molec. cm^{-2} and 3.2$\times 10^{14}$ molec. cm^{-2} and are close to the

546   range of expected uncertainties of stratospheric NO_2 estimates (Bucsela et al., 2013). The relative

547   differences in stratospheric NO_2 column between the two versions is close to 0% on average,

548   usually range between -2.5% and 2.0%, and occasionally reach up to ±13%. This difference in

549   stratospheric NO_2 estimates is much larger than the difference in stratospheric AMFs and is caused

550   by differences in tropospheric AMFs that influence NO_2 observations over unpolluted and cloudy

551   areas used by the stratosphere-troposphere separation scheme.

552   Figure 9 shows the seasonally averaged tropospheric NO_2 columns over the selected domains of

553   North America, Europe, southern Africa, and Asia for the months of June, July, and August in

554   2005. These domains contain highly polluted areas with significant NO_x emissions where the

555   impact of changes in surface reflectivity and cloud parameters on tropospheric NO_2 retrievals

556   becomes increasingly important. The use of more accurate pixel-specific information for surface

557   and cloud parameters in V4.0 results in significantly enhanced tropospheric NO_2 column retrievals

558   almost everywhere. The effect, however, varies with the vertical distribution of NO_2, with the

559   largest effects in high-column areas. This spatially-varying effect arising from algorithm changes

560   could have significant implications for estimates of trends and emissions of NO_x from satellite

561   observations.

562   Figure 10 shows the seasonal average tropospheric NO_2 columns for December through February.

563   While seasonal differences in NO_2 columns are evident owing to changes in NO_x lifetime and

564   boundary layer depth, the impact of algorithm changes in V4.0 remains similar. There are two

565   notable exceptions specifically related to observations over snow and ice surfaces. First, there are

566   significant data gaps in V3.1 but nearly none in V4.0. In V3.1, retrievals over snow and ice areas

567   were considered to be highly uncertain and therefore discarded, following the recommendation of

568   Boersma et al. (2011). As discussed above in Section 2.2.3, V4.0 incorporates changes in surface

569   and cloud treatment in NO_2 algorithm that allows us to retain more observations that we determine

570   to be our acceptable level of cloudiness. Next, these algorithm changes led to profound changes in

571   the calculated tropospheric AMFs and resulting NO_2 column amounts. The reduction in

572   tropospheric NO_2 retrievals in V4.0 over snow and ice covered surfaces arises from a combined

573   effect of enhanced values of surface reflectivity, their impact on the CRF and OCP retrievals, and

574   an inconsistent number of samples used in the calculation of the seasonal average. Nevertheless,

575   due to inferiority in the quality of BRDF data as well as complexities in separating snow from

576   clouds, caution is needed when interpreting winter time data at high latitudes.

577   Figure 11 shows some examples of how changes in the algorithm from V3.1 to V4.0 affect monthly
578   domain average tropospheric NO_2 columns over areas affected by various NO_x sources. In contrast
579   to minor changes over the pristine Pacific Ocean, month-to-month changes over source regions
580   vary considerably. The differences in tropospheric NO_2 columns between V4.0 and V3.1 range
581   from -11 to 15% over Beijing, China and from 0 to 29% over the Ruhr area in Germany, suggesting
582   variations in relative differences among cities and industrial areas. The changes over a major
583   biomass burning area of Democratic Republic of Congo, Angola, and Zambia range 13-56%
584   during the biomass burning season of May through August, but are <5% in other months.
585   Differences between the two versions are small over areas influenced by lightning NO_x emissions.
586

587   In Figure 12, we examine monthly variation of tropospheric NO_2 columns from the two versions
588   over five highly populated and polluted cities that vary in terrain types ranging from coastal (e.g.,
589   Shanghai, Tokyo) to mountainous (e.g., Mexico City). NO_2 columns in V4.0 are generally higher
590   than V3.1 by 0-30%, but the difference can occasionally reach up to 50% in some months. Changes
591   of that order of magnitude in highly polluted areas have implications for estimation of NO_x
592   emissions and trends using these data.

593   **3 Assessment of OMI NO_2 product**

594   In this section, we compare OMI NO_2 columns with total column retrievals from ground-based
595   Pandora measurements and integrated tropospheric columns from aircraft spirals at several
596   locations of the DISCOVER-AQ (Deriving Information on Surface Conditions from COlumn
597   and VERtically Resolved Observations Relevant to Air Quality) field campaign held between
598   2011 and 2014.

599   **3.1 Comparison between OMI and Pandora total column NO_2**

600   Here, we compare the total column NO_2 retrievals from OMI and the ground-based Pandora
601   spectrometer. Pandora is a compact sun-viewing remote sensing instrument that provides estimates
602   of NO_2 column amounts from the surface to the top of the atmosphere (Herman et al., 2009, 2018).
603   The NO_2 retrieval approach for Pandora is similar to that of OMI and consists of the DOAS spectral
604   fitting procedure to derive NO_2 SCD and its conversion to VCD using AMFs. However, the details

605 differ due to the lack of top-of-atmosphere radiance measurements for the spectral fitting and

606 simplicity in the AMF calculation for Pandora due to its direct sun measurements.

607 To compare with the OMI observations, we use Pandora data for sites listed in the Pandonia Global

608 Network (https://www.pandonia-global-network.org/). Out of 22 sites, we select 18 sites that we

609 determined to be suitable for comparison. Data from some of the sites (e.g., Rome, Italy) are

610 consistently higher than OMI by over a factor of two, suggesting that the sites may be in close

611 proximity to local sources that cannot be resolved by OMI. Although, some of the selected sites

612 have sporadic and short-term measurements (e.g., Ulsan, S. Korea), we consider them for

613 improved sampling and coverage. The collocation criteria include spatial and temporal matching

614 between OMI and Pandora observations by selecting the OMI pixels that encompass the Pandora

615 site and using Pandora 80-sec total NO_2 column data averaged over ± 10 minutes of OMI

616 observations. We use high quality data obtained under clear sky conditions with root-mean-square

617 of spectral fitting residuals < 0.05 and NO_2 retrieval uncertainty < 0.05 DU ($\sim 1.3 \times 10^{15}$ molec. cm-

618 ^{2}) for Pandora and with CRF < 0.5 for OMI.

619 Figure 13 shows a comparison of OMI total NO_2 columns (sum of tropospheric and stratospheric

620 columns) with coincidently sampled Pandora direct-sun NO_2 column retrievals at a clean site of

621 Izaña in Tenerife Island, Spain, and a more polluted site in Greenbelt (Maryland, USA). The Izaña

622 Atmospheric Observatory is located on the top of a mountain plateau, with an elevation of 2373

623 meters above sea level. Since the site is free of local anthropogenic influences, Pandora

624 observations likely provide stratospheric and free tropospheric NO_2 amounts. In contrast, the

625 Greenbelt site in a suburban Washington DC area has traffic and air quality typical of polluted US

626 cities. As shown in Figures 13(a) and 13(b), OMI NO_2 retrievals from the two versions are highly

627 consistent (r>0.92) with somewhat higher values in V4.0 as compared to V3.1, by on average 13%

628 in Greenbelt and just 1% in Izaña. The variations of OMI NO_2 from both versions are also broadly

629 consistent with the Pandora measurements. The OMI and Pandora NO_2 columns are fairly

630 correlated (r = 0.32, N = 232) at Izaña, and moderately correlated (r = 0.51, N = 123) at Greenbelt;

631 often times the differences between each individual OMI and Pandora observations are significant.

632 Overall, the total column NO_2 data from OMI is higher than Pandora, with the average difference

633 of <16%. Occasional large discrepancies between OMI and Pandora reflect a combination of

spatial heterogeneity, differences in spatial and temporal sampling, differences in vertical sensitivity of satellite and ground-based observations, and errors in OMI and Pandora retrievals. Figures 13(c) and 13(d) show the multi-year monthly mean variation of OMI and Pandora NO_2 columns. The seasonal variation in Pandora and OMI NO_2 columns is highly consistent and exhibits a summer maximum and a fall minimum at Izaña, and a winter maximum and summer minimum in Greenbelt. The seasonal variation in the total column reflects that of the stratosphere for Izaña and of the troposphere in Greenbelt. For Izaña, the monthly mean differences between OMI and Pandora range from 8.2% in June to 38% in October for V4.0 and from 7.0% in June to 37% in October for V3.1. This discrepancy is likely due to the large aerial coverage of OMI pixels including nearby cities, unlike the point measurements made by Pandora at the mountain top. The average tropospheric NO_2 column observed by OMI is 8.9×10^{14} molec cm^{-2}, suggesting significant NO_2 amounts in the troposphere with 20-32% contributions to total column NO_2 on a monthly scale. For Greenbelt, the monthly mean differences between OMI and Pandora are within $\pm12\%$ for the majority of the cases for both versions, with V4.0 improving agreement for February, April, May and December, and worsening somewhat in other months, especially in September and November, when the two versions exhibit larger differences in tropospheric NO_2 retrievals.

Figure 14 shows average total NO_2 columns measured by Pandora and OMI at the 18 selected sites. Although there is a wide range of differences between individual sites, Pandora and OMI observations exhibit a good spatial correlation, with slightly improved correlation for V4.0 (r=0.65, N=1082) as compared to V3.1 (r=0.62). The site-specific average values generally agree to $\pm35\%$ for columns $< 10^{16}$ molec. cm^{-2}. For more polluted sites, OMI retrievals tend to be lower than the Pandora data. Although the relationship between Pandora and OMI has not changed appreciably with the updates made in the OMI V4.0 product, the corrections are in the right direction for a majority of the sites. The observed differences should not be interpreted as biases in retrievals but rather as the combined effect of differences in spatial coverage, heterogeneity in the NO_2 field, preferential placement of Pandora instruments, and potentially, a lack of site-specific profile shapes assumed in OMI retrievals.

3.2 Assessment using DISCOVER-AQ observations

We also use NO_2 observations from the DISCOVER-AQ field program to assess V4.0 OMI NO_2 retrievals. The DISCOVER-AQ campaign was composed of four field deployments: Baltimore-Washington area in Maryland (MD) in July 2011; the San Joaquin Valley in California (CA) in

665 January-February 2013; Houston, Texas (TX) in September 2013; and Denver, Colorado (CO) in
666 July-August 2014. An observing strategy of the campaign was to carry out systematic and
667 concurrent in situ and remote sensing observations from a network of ground sites and research
668 aircraft that spiraled over each site 2-4 times a day. The payload of the P-3B research aircraft
669 included in situ measuring instruments to measure NO_2 profiles in the 0.3-5 km altitude range.
670 Each campaign hosted ground-based networks of surface monitors to provide in situ NO_2
671 observations as well as Pandora spectrometers to measure NO_2 column amounts.

672 We use Pandora NO_2 column observations and in situ NO_2 spiral data spatially and temporally
673 matched to OMI on clear and partially cloudy (cloud radiance fraction < 0.5) days. Airborne
674 measurements were carried out using the 4-channel chemiluminescence instrument from the
675 National Center for Atmospheric Research (Ridley and Grahek, 1990) and the Thermal
676 Dissociation Laser-Induced Florescence from the University of Berkeley (Thornton et al., 2000).
677 Despite differences in the measurement technique and sampling strategy, NO_2 measurements from
678 the two instruments are highly consistent and generally agree within 10%, with the exception of
679 ~32% difference for Houston (Choi et al., 2020). Here, we use the 1-second merged data from the
680 chemiluminescence instrument only, taking advantage of its high frequency measurements. The
681 spiral data are extended to the ground by using coincident in situ surface NO_2 measurements
682 sampled over the duration of spiral (~20 minutes). To account for NO_2 amounts in the missing
683 portion from the highest aircraft altitude to the tropopause, we use NO_2 from the GMI simulation.
684 Like the surface data, the Pandora total column NO_2 data are averaged over the duration of each
685 aircraft spiral. For OMI, we include data from all cross-track positions that are not subject to the
686 row anomaly.

687 Figure 15 and Table 2 show a summary of the comparison of OMI V4.0 NO_2 columns with
688 vertically integrated tropospheric columns from the P-3B aircraft at 20 spiral locations. Overall,
689 tropospheric NO_2 columns from OMI and aircraft spirals suggest a poor agreement but a good
690 correlation (r=0.74, N=100), although the agreement and correlations vary by campaign locations
691 (r=0.4 for MD to r=0.81 for CA). OMI retrievals are usually lower than the aircraft data, with
692 larger differences for sites with larger NO_2 gradients and columns (e.g., Denver La Casa, CO;
693 Fresno, CA). OMI is rarely higher than the aircraft data as this usually happens over relatively
694 cleaner sites (e.g., Fairhill, MD). This alternating nature of the variation in results in polluted
695 versus clean areas suggests that OMI's large footprint size and narrow spiral radius (~4 km) of the

696   aircraft are likely the primary cause for the observed differences. This was demonstrated in Choi

697   et al. (2020) by using high-resolution Community Multi-scale Air Quality Model (CMAQ)

698   simulations. Additional contributions to the observed differences could come from OMI retrieval

699   errors arising from the use of a coarse resolution GMI-based a priori NO_2 profile shapes in the

700   AMF calculation. Such profile-related retrieval errors can be partially accounted for by replacing

701   GMI profiles with the aircraft observed NO_2 profiles (OMI_{obs}). The use of observed profiles in the

702   OMI retrievals leads to a slight change in correlation, but 20-35% reduction in mean difference

703   between OMI and aircraft observations, highlighting the role of a priori profiles in NO_2 retrievals

704   as suggested by previous studies (Russell et al., 2011; Lamsal et al., 2014; Goldberg et al., 2017;

705   Laughner et al., 2019; Choi et al., 2020). The campaign-average difference between OMI and

706   aircraft observations is -23.1%. We note here that the aircraft observed profiles can be very

707   different from the actual profiles over OMI's FOVs (pixels) due to a difference in the sampling

708   domains for the two measurements.

709   Figure 15 and Table 2 also show the comparison between the OMI and Pandora total column

710   retrievals at the 20 DISCOVER-AQ sites. The correlation between collocated OMI and Pandora

711   observations for individual campaign locations vary from fair (r=0.13 for MD) to good (r=0.70 for

712   CO), with a moderate correlation (r=0.56, N=83) for all observations from the four locations. As

713   compared to the aircraft observations, the OMI data generally show better agreement with the

714   Pandora retrievals, with the smallest difference in MD and the largest difference in CO. The use

715   of aircraft-observed NO_2 profiles in AMF calculations leads to higher OMI column retrievals than

716   those from Pandora for MD and TX, and lower columns than Pandora for CA and CO. Overall,

717   total column retrievals from OMI are 16.3% lower than Pandora. The observed discrepancy

718   between the OMI, aircraft spiral, and Pandora data points to general difficulties in comparing

719   observations of different spatial resolutions for a short-lived trace gas like NO_2 that has large

720   spatial gradients, especially in the boundary layer.

721   **4 Conclusions**

722   We have described a series of significant improvements made to the operational OMI NO_2

723   Standard Product (OMNO2) algorithm. The new version, version 4.0 (V4.0), of the OMNO2

724   product, released recently to the public at the NASA Goddard Earth Sciences Data and Information

725   Services Center (GES DISC), mainly relies on improved methods and high-resolution inputs for a

726   more accurate determination of air mass factors (AMFs). Major improvements include (1) a new

727 O$_2$-O$_2$ cloud algorithm to estimate cloud radiance fraction (CRF) and cloud optical centroid

728 pressure (OCP), both required for the AMF calculation; 2) a new MODIS BRDF-derived

729 geometry-dependent surface Lambertian Equivalent Reflectivity (GLER) input data used in both

730 the NO$_2$ and cloud retrievals; (3) improved terrain pressure calculated for OMI's footprint; and (4)

731 improved surface and cloud treatments over snow and ice surfaces. Over open-water areas, inputs

732 to the GLER calculations include chlorophyll concentrations from MODIS, the wind speed data

733 from the Advanced Microwave Scanning Radiometer–Earth Observing System (AMSR-E) and

734 the Special Microwave Imager–Sounder (SSMIS) instruments, and the wind direction data from

735 the NASA GEOS-5 model. The following algorithmic steps remain unchanged: the scheme for

736 separating stratospheric and tropospheric components, first implemented in Version 2.1 (Bucsela

737 et al., 2013; Lamsal et al., 2014); an optimized spectral fitting algorithm used for NO$_2$ slant column

738 density retrievals (Marchenko et al., 2015); and the use of annually varying monthly mean Global

739 Modeling Initiative (GMI) derived inputs (e.g., NO$_2$ vertical profile shapes), as implemented in

740 Version 3.0 (Krotkov et al., 2017).

741 The changes in inputs result in substantial changes tropospheric AMFs (and thus VCDs) in V4.0

742 relative to the previous version (V3.1). The geometry-dependent GLER data computed for OMI

743 observations used in V4.0 differ considerably from the OMI-derived climatological LER data

744 (Kleipool et al., 2008) used in V3.1. The data from GLER (a unitless value with 0.0-1.0 range) are

745 generally lower, by <0.05, than the climatological LER data over land and ocean outside of

746 sunglint areas; GLER is much higher over the sunglint areas that reaches more than 0.3 due to the

747 geometry-dependent Fresnel reflection. The cloud parameters (OCP and CRF) retrieved from by

748 new O$_2$-O$_2$ cloud algorithm described here and those from the operational cloud algorithm

749 (Veefkind et al., 2016) used in V3.1 exhibit significant differences with generally larger values for

750 both parameters in V4.0 as compared to V3.1, with noticeable exceptions over sunglint areas,

751 where CRFs in V4.0 are lower than V3.1 by <0.3. Over snow and ice surfaces, identified by the

752 Near-real-time Ice and Snow Extent (NISE) flags in the OMI L1b data, various adjustments are

753 made in V4.0 for GLER, OCP, and CRF by using other diagnostic parameters (e.g., scene pressure)

754 retrieved by the new cloud algorithm. The scattering weights and tropospheric AMFs for NO$_2$

755 respond to the changes in these input parameters in a complicated way. Typically, tropospheric

756 AMFs decrease with the use of GLER and increase with the use of the new cloud parameters, with

757 exceptions over water surfaces affected by sunglint, where we observe the opposite effect. Over

758 highly polluted areas, the effect from GLER is augmented by the effect from the new cloud

759 parameters, resulting in a considerable decrease in the tropospheric AMF. Changes in tropospheric

760 AMFs resulting from the updates in treatment of the snow and ice-covered areas are also

761 significant. Changes in the adopted terrain pressure (V4.0 vs V3.1) can also have a sizable effect

762 on tropospheric AMFs, particularly over areas with a complex terrain. In contrast, for stratospheric

763 AMFs the combined impact of all of these algorithmic updates is negligible.

764 The changes in tropospheric AMFs translate directly into changes in tropospheric NO_2 retrievals

765 and indirectly into stratospheric NO_2 estimates. Over background and low column NO_2 areas,

766 tropospheric NO_2 column estimates have not changed appreciably from V3.1 to V4.0. Over more

767 polluted areas, the tropospheric NO_2 retrievals have typically increased by 10-40% from V3.1 to

768 V4.0, mostly in a direct proportion to the pollution level. Most of the increase in the highly polluted

769 areas is driven by the change in the surface reflectivity data used in the AMF calculation, with

770 additional increase due to changes in the cloud parameters. Changes in the stratospheric NO_2

771 estimates are usually within ±2.5%, which is close to the range of estimated uncertainties of

772 stratospheric NO_2 estimates.

773 A global assessment of V4.0 tropospheric and stratospheric NO_2 products was performed by a

774 thorough evaluation of their consistency with the data from V3.1, which was carefully evaluated

775 in our previous works (e.g., Krotkov et al., 2017; Choi et al., 2020). In addition, we use

776 NO_2 measurements made by independent ground- and aircraft-based instruments to evaluate the

777 V4.0 product. The comparison of OMI total column NO_2 data with collocated Pandora

778 observations at its 18 global network and 20 DISCOVER-AQ locations suggests that OMI and

779 Pandora are generally highly consistent, exhibit similar seasonal variation, and agree within their

780 expected uncertainties of 2.7×10^{15} molec cm^{-2} for Pandora (Herman et al., 2009) and ~30% for

781 OMI under clear-sky conditions (Boersma et al., 2011; Bucsela et al., 2013). Individual data points

782 differ considerably, and OMI tends to be lower than Pandora over highly polluted areas with

783 spatially inhomogeneous NO_2. The comparison of OMI tropospheric NO_2 column retrievals with

784 columns derived from the aircraft spirals and surface data during the DISCOVER-AQ campaign

785 also suggests general agreement in spatial variation, but OMI values are about a factor of two

786 lower in polluted environments. This difference is due partly to inaccurate a priori assumptions,

787 but primarily to OMI's relatively large pixels. The use of observed NO_2 profiles as a priori

788 information reduces the bias from ~50% to 23%, on average. The Multiple-Axis Differential

789   Optical Absorption Spectrometer (MAX-DOAS) (e.g., Chan et al., 2019) or high spatial resolution

790   measurements from aircraft (e.g., Nowlan et al., 2016; Lamsal et al., 2017; Judd et al., 2019) would

791   provide a more comprehensive validation by mapping the NO_2 distributions over the complete

792   areas of aircraft spirals and the satellite FOVs.

793   In this study, we focused on improving the surface and cloud parameters in the NASA standard

794   NO_2 product retrievals. To further improve the retrieval accuracy, it is important to incorporate

795   improved retrieval methods and auxiliary information, such as high resolution a priori NO_2

796   profiles. For instance, current cloud algorithms based on the MLER model treat aerosols implicitly

797   by providing effective (cloud + aerosol) CRF and effective cloud OCP, both necessary inputs for

798   AMF calculations. Cloud effects on trace gas retrievals can be compromised by the unknown

799   aerosol effects, which lead to errors in AMF calculations. Therefore, the use of the GLER product

800   in the NO_2 algorithm will greatly benefit from an explicit accounting for aerosol effects,

801   particularly over polluted regions. We have recently developed an explicit and consistent aerosol

802   correction method which can be applied consistently in both the cloud and NO_2 retrievals

803   (Vasilkov et al. 2020); it uses a model of the aerosol optical properties from a global aerosol

804   assimilation system paired with radiative transfer calculations. This approach allows us to account

805   for aerosols within the OMI cloud and NO_2 algorithms with relatively small changes and will be

806   used in the next version of the NO_2 algorithm.

807

808   **Code/Data availability:** The Level-2 swath type column NO_2 products (OMNO2) is available

809   from the NASA Goddard Earth Sciences Data and Information Services Center (GES DISC)

810   website (https://disc.gsfc.nasa.gov/datasets/OMNO2G_003/summary). Other OMNO2-associated

811   NO_2 products such as the Level-2 gridded column product, OMNO2G, and the Level-3 gridded

812   column product, OMNO2d, both sampled at regular 0.25° latitude x 0.25° longitude wide grids are

813   distributed   through   the   NASA   GES-DISC

814   (https://disc.gsfc.nasa.gov/datasets/OMNO2d_003/summary)   and   GIOVANNI

815   (https://giovanni.gsfc.nasa.gov/giovanni/) websites. An additional high spatial resolution (0.1° x

816   0.1° latitude-longitude grid) OMNO2d product (OMNO2d_HR) is also made available through

817   the   NASA   AVDC   website

818   (https://avdc.gsfc.nasa.gov/pub/data/satellite/Aura/OMI/V03/L3/OMNO2d_HR/).   The   AVDC

819   website also hosts overpass files for several hundred sites around the globe

820   (https://avdc.gsfc.nasa.gov/pub/data/satellite/Aura/OMI/V03/L2OVP/OMNO2/).

821

822   *Author contributions.* LNL, NAK, JJ, and AV designed the data analysis. WQ, ZF, NAK, DH,

823   and AV developed and evaluated the GLER product. EY, SM, AV, NAK, JJ, and BF developed

824   and evaluated the cloud product. LNL, NAK, SM, WHS, and EB have developed and evaluated

825   the NASA NO_2 Standard Product. LNL and SC conducted validation of the OMI NO_2 products

826   using Pandora and other independent observations. LNL, AV, SM, and ZF wrote the manuscript

827   with comments from all coauthors.

828

829   *Competing interests.* The authors declare no competing interests.

830

831   *Acknowledgements.* We acknowledge the NASA Earth Science Division for funding OMI NO_2

832   product development and analysis. The Dutch–Finnish-built OMI instrument is part of the NASA

833   EOS Aura satellite payload. KNMI and the Netherlands Space Agency (NSO) manage the OMI

834   project. We acknowledge the NASA Pandora, ESA-Pandonia, and NASA's DISCOVER-AQ

835   projects for free access to the data. We thank the two anonymous reviewers for their helpful

836   comments.

837

References

Beirle, S., Boersma, K. F., Platt, U., Lawrence, M. G., and Wagner, T.: Megacity emissions and lifetimes of nitrogen oxides probed from space, *Science*, *333*, 1737–1739. https://doi.org/10.1126/science.1207824, 2011.

Berezin, E. V, Konovalov, I. B., Ciais, P., Richter, A., Tao, S., Janssens-Maenhout, G., et al.: Multiannual changes of CO_2 emissions in China: indirect estimates derived from satellite measurements of tropospheric NO_2 columns, *Atmos. Chem. Phys*, *13*, 9415–9438. https://doi.org/10.5194/acp-13-9415-2013, 2013.

Boersma, K. F., Eskes, H. J., Dirksen, R. J., van der A, R. J., Veefkind, J. P., Stammes, P., Huijnen, V., Kleipool, Q. L., Sneep, M., Claas, J., Leitão, J., Richter, A., Zhou, Y., and Brunner, D.: An improved tropospheric NO_2 column retrieval algorithm for the Ozone Monitoring Instrument, *Atmos. Meas. Tech.*, 4, 1905–1928, https://doi.org/10.5194/amt-4-1905-2011, 2011.

Boersma, K. F., Eskes, H. J., Richter, A., De Smedt, I., Lorente, A., Beirle, S., van Geffen, J. H. G. M., Zara, M., Peters, E., Van Roozendael, M., Wagner, T., Maasakkers, J. D., van der A, R. J., Nightingale, J., De Rudder, A., Irie, H., Pinardi, G., Lambert, J.-C., and Compernolle, S. C.: Improving algorithms and uncertainty estimates for satellite NO_2 retrievals: results from the quality assurance for the essential climate variables (QA4ECV) project, *Atmos. Meas. Tech.*, 11, 6651–6678, https://doi.org/10.5194/amt-11-6651-2018, 2018.

Bucsela, E.J., Celarier, E.A., Wenig, M.O., Gleason, J.F., Veefkind, J.P., Boersma, K.F., and Brinksma, E.J.: Algorithm for NO_2 vertical column retrieval from the Ozone Monitoring Instrument, *IEEE Trans. Geosci. Remote Sens.*, 44, 5, 2006.

Bucsela, E. J., Krotkov, N. A., Celarier, E. A., Lamsal, L. N., Swartz, W. H., Bhartia, P. K., Boersma, K. F., Veefkind, J. P., Gleason, J. F., and Pickering, K. E.: A new stratospheric and tropospheric NO_2 retrieval algorithm for nadir-viewing satellite instruments: applications to OMI, *Atmos. Meas. Tech.*, 6, 2607–2626, https://doi.org/10.5194/amt-6-2607-2013, 2013.

Cai, K., Li, S., Zheng, F., Yu, C., Zhang, X., Liu, Y., and Li, Y.: Spatio-temporal Variations in NO_2 and $PM_{2.5}$ over the Central Plains Economic Region of China during 2005-2015 Based on Satellite Observations, *Aer. Air Qual. Res.*, 5, 1221–1235, 10.4209/aaqr.2017.10.0394, 2018.

Canty, T. P., Hembeck, L., Vinciguerra, T. P., Anderson, D. C., Goldberg, D. L., Carpenter, S.

F., Allen, D. J., Loughner, C. P., Salawitch, R. J., and Dickerson, R. R.: Ozone and NO_x chemistry in the eastern US: evaluation of CMAQ/CB05 with satellite (OMI) data, *Atmos. Chem. Phys.*, 19, 10965–10982, 10.5194/acp-15-10965-2015, 2015.

Castellanos, P., and Boersma, K. F.: Reductions in nitrogen oxides over Europe driven by environmental policy and economic recession, *Sci. Rep.*, 1, 10.1038/srep00265, 2012.

Celarier, E. A., et al: Validation of Ozone Monitoring Instrument nitrogen dioxide columns, *J. Geophys. Res.*, 113, D15S15, doi:10.1029/2007JD008908, 2008.

Chance, K., Kurosu, T.P., and Sioris, K.E.: Undersampling correction for array detector-based satellite spectrometers, *Appl. Opt.*, 44, 1296– 1304, 2005.

Chan, K. L., Wang, Z., Ding, A., Heue, K.-P., Shen, Y., Wang, J., Zhang, F., Shi, Y., Hao, N., and Wenig, M.: MAX-DOAS measurements of tropospheric NO_2 and HCHO in Nanjing and a comparison to ozone monitoring instrument observations, *Atmos. Chem. Phys.*, 19, 10051– 10071, https://doi.org/10.5194/acp-19-10051-2019, 2019.

Choi, S., Lamsal, L. N., Follette-Cook, M., Joiner, J., Krotkov, N. A., Swartz, W. H., Pickering, K. E., Loughner, C. P., Appel, W., Pfister, G., Saide, P. E., Cohen, R. C., Weinheimer, A. J., and Herman, J. R.: Assessment of NO_2 observations during DISCOVER-AQ and KORUS-AQ field campaigns, Atmos. Meas. Tech., 13, 2523–2546, https://doi.org/10.5194/amt-13-2523-2020, 2020.

Cooper, M.J., Martin, R.V., Lyapustin, A.I., and McLinden, C.A.: Assessing snow extent data sets over North America to inform and improve trace gas retrievals from solar backscatter, *Atmos. Meas. Tech.*, 11, 2983-2994, https://doi.org/10.5194/amt-11-2983-2018, 2018.

Cox, C. and Munk, W.: Statistics of the sea surface derived from sun glitter, *J. Mar. Res.*, 13, 198– 227, 1954.

de Foy, B., Lu, Z., Streets, D. G., Lamsal, L. N., and Duncan, B. N.: Estimates of power plant NO_x emissions and lifetimes from OMI NO_2 satellite retrievals. *Atmos. Environ.*, *116*, 1–11, https://doi.org/10.1016/j.atmosenv.2015.05.056, 2015.

Dirksen, R., Dobber, M., Voors, R, and Levelt, P.: Prelaunch characterization of the Ozone Monitoring Instrument transfer function in the spectral domain, *Appl. Opt.*, 45, 3972– 3981, 2006.

Dix, B., Bruin, J., Roosenbrand, E., Vlemmix, T., Francoeur, C., Gorchov-Negron, A., McDonald, B., Zhizhin, M., Elvidge, C., Veefkind, P., Levelt, P., and de Gouw,

900   J.: Nitrogen Oxide Emissions from U.S. Oil and Gas Production: Recent Trends and Source

901   Attribution, *Geophys. Res. Lett.*, 1, e2019GL085866, 10.1029/2019gl085866, 2020.

902   Dobber, M., Kleipool, Q., Dirksen, R., Levelt, P. F., Jaross, G., Taylor, S., et al.: Validation of

903   Ozone Monitoring Instrument level 1b data products. *J. Geophys. Res.*,

904   https://doi.org/10.1029/2007JD008665, 2008.

905   Douglass, A. R., Stolarski, R.S., Strahan, S.E., and Connell, P.S.: Radicals and reservoirs in the

906   GMI chemistry and transport model: Comparison to measurements, *J. Geophys. Res.*, 109,

907   D16302, doi:10.1029/2004JD004632, 2004.

908   Duncan, B. N., Yoshida, Y., Foy, B., Lamsal, L. N., Streets, D. G., Lu, Z., Pickering, K. E., and

909   Krotkov, N. A.: The observed response of Ozone Monitoring Instrument (OMI) NO_2 columns

910   to NOx emission controls on power plants in the United States: 2005–2011, *Atmos. Environ.*,

911   102–111, 10.1016/j.atmosenv.2013.08.068, 2013.

912   Duncan, B.N., Lamsal, L.N., Thompson, A.M., Yoshida, Y., Lu, Z., Streets, D.G., Hurwitz, M.M.,

913   Pickering, K.E.: A space-based, high-resolution view of notable changes in urban NO_x

914   pollution around the world (2005-2014), *J. Geophys. Res.*, 121, 976–996,

915   doi:10.1002/2015JD024121, 2016.

916   Eskes, H. J. and Boersma, K. F.: Averaging kernels for DOAS total-column satellite retrievals,

917   *Atmos. Chem. Phys.*, 3, 1285–1291, https://doi.org/10.5194/acp-3-1285-2003, 2003.

918   Fasnacht, Z., Vasilkov, A., Haffner, D., Qin, W., Joiner, J., Krotkov, N., Sayer, A. M., and Spurr,

919   R.: A geometry-dependent surface Lambertian-equivalent reflectivity product for UV–Vis

920   retrievals – Part 2: Evaluation over open ocean, *Atmos. Meas. Tech.*, 12, 6749–6769,

921   https://doi.org/10.5194/amt-12-6749-2019, 2019.

922   Geddes, J. A. and Martin, R. V.: Global deposition of total reactive nitrogen oxides from 1996 to

923   2014 constrained with satellite observations of NO_2 columns, *Atmos. Chem. Phys.*, 17,

924   10071–10091, https://doi.org/10.5194/acp-17-10071-2017, 2017.

925   Gelaro, R., McCarty, W., Suárez, M.J., Todling, R., Molod, A., Takacs, L., Randles, C.A.,

926   Darmenov, A., Bosilovich, M.G., Reichle, R., Wargan, K., Coy, L., Cullather, R., Draper, C.,

927   Akella, S., Buchard, V., Conaty, A., da Silva, A.M., Gu, W., Kim, G., Koster, R., Lucchesi,

928   R., Merkova, D., Nielsen, J.E., Partyka, G., Pawson, S., Putman, W., Rienecker, M., Schubert,

929   S.D., Sienkiewicz, M., and Zhao, B.: The Modern-Era Retrospective Analysis for Research

930   and Applications, Version 2 (MERRA-2). *J. Climate,* 30, 5419–

5454, https://doi.org/10.1175/JCLI-D-16-0758.1, 2017.

Ghude, S. D., Kulkarni, S. H., Jena, C., Pfister, G. G., Beig, G., Fadnavis, S., and A, R. J.: Application of satellite observations for identifying regions of dominant sources of nitrogen oxides over the Indian Subcontinent, *J. Geophys. Res.*, 2, 1075–1089, 10.1029/2012jd017811, 2013.

Goldberg, D. L., Lamsal, L. N., Loughner, C. P., Swartz, W. H., Lu, Z., and Streets, D. G.: A high-resolution and observationally constrained OMI NO_2 satellite retrieval. *Atmos. Chem. Phys.*, *17*, 11403–11421. https://doi.org/10.5194/acp-17-11403-2017, 2017.

Goldberg, D. L., Saide, P. E., Lamsal, L. N., de Foy, B., Lu, Z., Woo, J.-H., et al.: A top-down assessment using OMI NO_2 suggests an underestimate in the NO_x emissions inventory in Seoul, South Korea, during KORUS-AQ. *Atmos. Chem. Phys.*, *19*, 1801–1818. https://doi.org/10.5194/acp-19-1801-2019, 2019a.

Goldberg, D., Lu, Z., Oda, T., Lamsal, L.N, Liu, F., Griffin, D., McLinden, C., Krotkov, N.A., Duncan, B.N., Streets, D.: Exploiting OMI NO_2 satellite observations to infer fossil-fuel CO_2 emissions from U.S. megacities, *Sci. Tot. Environ.*, 695, 133805, 10.1016/j.scitotenv.2019.133805, 2019b.

Gu, J., Chen, L., Yu, C., Li, S., Tao, J., Fan, M., Xiong, X., Wang, Z., Shang, H., and Su, L.: Ground-Level NO_2 Concentrations over China Inferred from the Satellite OMI and CMAQ Model Simulations, *Rem. Sens.*, 6, 519, 10.3390/rs9060519, 2017.

Han, K., Lee, C., Lee, J., Kim, J., and Song, C.: A comparison study between model-predicted and OMI-retrieved tropospheric NO_2 columns over the Korean peninsula, *Atmos. Environ.*, 17, 2962–2971, 10.1016/j.atmosenv.2010.10.016, 2011.

Herman, J., Cede, A., Spinei, E., Mount, G., Tzortziou, M., and Abuhassan, N.: NO_2 column amounts from ground-based Pandora and MFDOAS spectrometers using the direct-sun DOAS technique: Intercomparisons and application to OMI validation, *J. Geophys. Res. Atmos.*, 114, D13, https://doi.org/10.1029/2009JD011848, https://agupubs.onlinelibrary.wiley.com/doi/abs/10.1029/2009JD011848, 2009.

Herman, J., Spinei, E., Fried, A., Kim, J., Kim, J., Kim, W., Cede, A., Abuhassan, N., and Segal-Rozenhaimer, M.: NO_2 and HCHO measurements in Korea from 2012 to 2016 from Pandora spectrometer instruments compared with OMI retrievals and with aircraft measurements during the KORUS-AQ campaign, *Atmos. Meas. Tech.*, 11, 4583–4603,

https://doi.org/10.5194/amt-11-4583-2018, https: //www.atmos-meas-tech.net/11/4583/2018/, 2018.

Herron-Thorpe, F. L., Lamb, B. K., Mount, G. H., and Vaughan, J. K.: Evaluation of a regional air quality forecast model for tropospheric NO_2 columns using the OMI/Aura satellite tropospheric NO_2 product, *Atmos. Chem. Phys.*, 18, 8839–8854, 10.5194/acp-10-8839-2010, 2010.

Hudman, R. C., Moore, N. E., Mebust, A. K., Martin, R. V., Russell, A. R., Valin, L. C., and Cohen, R. C.: Steps towards a mechanistic model of global soil nitric oxide emissions: implementation and space based-constraints, *Atmos. Chem. Phys.*, 16, 7779–7795, 10.5194/acp-12-7779-2012, 2012.

Ialongo, I., Herman, J., Krotkov, N., Lamsal, L., Boersma, K. F., Hovila, J., and Tamminen, J.: Comparison of OMI NO_2 observations and their seasonal and weekly cycles with ground-based measurements in Helsinki, *Atmos. Meas. Tech.*, 10, 5203–5212, 10.5194/amt-9-5203-2016, 2016.

Joiner, J., Bhartia, P., Cebula, R., Hilsenrath, E., McPeters, R., and Park, H.: Rotational Raman scattering (Ring effect) in satellite backscatter ultraviolet measurements, *Appl. Opt.*, 34, 4513-4525, 1995.

Joiner J. and Vasilkov, A. P.: First Results from the OMI Rotational-Raman Scattering Cloud Pressure Algorithm, *IEEE Trans. Geophys. Remote Sens.,* 44, 1272–1282, 2006.

Joiner, J., Vasilkov, A. P., Gupta, P., Bhartia, P. K., Veefkind, P., Sneep, M., de Haan, J., Polonsky, I., and Spurr, R.: Fast simulators for satellite cloud optical centroid pressure retrievals; evaluation of OMI cloud retrievals, *Atmos. Meas. Tech.*, 5, 529–545, https://doi.org/10.5194/amt-5-529-2012, 2012.

Judd, L. M., Al-Saadi, J. A., Janz, S. J., Kowalewski, M. G., Pierce, R. B., Szykman, J. J., Valin, L. C., Swap, R., Cede, A., Mueller, M., Tiefengraber, M., Abuhassan, N., and Williams, D.: Evaluating the impact of spatial resolution on tropospheric NO_2 column comparisons within urban areas using high-resolution airborne data, *Atmos. Meas. Tech.,* 12, 6091–6111, https://doi.org/10.5194/amt-12-6091-2019, 2019.

Kim, H. C., Lee, P., Judd, L., Pan, L., and Lefer, B.: OMI NO_2 column densities over North American urban cities: the effect of satellite footprint resolution, *Geos. Mod. Develop.*, 3, 1111–1123, 10.5194/gmd-9-1111-2016, 2016.

993   Kleipool, Q. L., Dobber, M. R., de Haan, J. F., and Levelt, P. F.: Earth surface reflectance
994   climatology from 3 years of OMI data, *J. Geophys. Res.*, 113, D18308,
995   doi:10.1029/2008JD010290, 2008.

996   Koelemeijer, R. B. A., Stammes, P., Hovenier, J. W., and de Haan, J. F.: A fast method for
997   retrieval of cloud parameters using oxygen A-band measurements from the Global Ozone
998   Monitoring Experiment, *J. Geophys. Res.,* 106, 3475–3496, 2001.

999   Konovalov, I. B., Berezin, E. V., Ciais, P., Broquet, G., Zhuravlev, R. V., and Janssens-Maenhout,
1000   G.: Estimation of fossil-fuel CO_2 emissions using satellite measurements of "proxy" species.
1001   *Atmos. Chem. Phys.*, *16*(21), 13509–13540. https://doi.org/10.5194/acp-16-13509-2016,
1002   2016.

1003   Krotkov, N. A., McLinden, C. A., Li, C., Lamsal, L. N., Celarier, E. A., Marchenko, S.
1004   V., Swartz, W. H., Bucsela, E. J., Joiner, J., Duncan, B. N., Boersma, K..F., Pepijn, J.P.,
1005   Levelt, P.F., Fioletov, V.E., Dickerson, R. R., He, H., Lu, Z., and D. G. Streets, D.G.: Aura
1006   OMI observations of regional SO_2 and NO_2 pollution changes from 2005 to 2015, *Atmos.*
1007   *Chem. Phys.*, 7, 4605–4629, 10.5194/acp-16-4605-2016, 2016.

1008   Krotkov, N. A., Lamsal, L. N., Celarier, E. A., Swartz, W. H., Marchenko, S. V., Bucsela, E. J., et
1009   al.: The version 3 OMI NO_2 standard product. *Atmos. Meas. Tech.*, *10*, 3133–3149.
1010   https://doi.org/10.5194/amt-10-3133-2017, 2017.

1011   Kuhlmann, G., Lam, Y. F., Cheung, H. M., Hartl, A., Fung, J. C. H., Chan, P. W., and Wenig, M.
1012   O.: Development of a custom OMI NO_2 data product for evaluating biases in a regional
1013   chemistry transport model, *Atmos. Chem. Phys*., 15, 5627–5644, https://doi.org/10.5194/acp-
1014   15-5627-2015, 2015.

1015   Lamsal, L.N., Martin, R.V., van Donkelaar, A., Celarier, E.A., Bucsela, E.J., Boersma, K.F.,
1016   Dirksen, R., Luo, C., and Wang, Y.: Indirect validation of tropospheric nitrogen dioxide
1017   retrieved from the OMI satellite instrument: Insight into the seasonal variation of nitrogen
1018   oxides at northern midlatitude, *J. Geophys. Res*., 115, doi:10.1029/2009JD013351, 2010.

1019   Lamsal, L.N., Martin, R.V., Parrish D.D., and Krotkov, N.A.: Scaling relationship for NO_2
1020   pollution and population size: A satellite perspective, *Environ. Sci. Technol*, 47, 7855-7861,
1021   2013.

1022   Lamsal, L. N., Krotkov, N. A., Celarier, E. A., Swartz, W. H., Pickering, K. E., Bucsela, E. J.,
1023   Gleason, J. F., Martin, R. V., Philip, S., Irie, H., Cede, A., Herman, J., Weinheimer, A.,

Szykman, J. J., and Knepp, T. N.: Evaluation of OMI operational standard NO_2 column retrievals using in situ and surface-based NO_2 observations, *Atmos. Chem. Phys.*, 14, 11587–11609, https://doi.org/10.5194/acp-14-11587-2014, 2014.

Lamsal, L.N., Duncan, B.N., Yoshida, Y., Krotkov, N.A., Pickering, K.E., Streets, D.G., Lu, Z.: U.S. NO_2 trends (2005–2013): EPA Air Quality System (AQS) data versus improved observations from the Ozone Monitoring Instrument (OMI), *Atmos. Env.*, 110, pp:130-143, doi:10.1016/j.atmosenv.2015.03.055, 2015.

Laughner, J. L., Zhu, Q., and Cohen, R. C.: Evaluation of version 3.0B of the BEHR OMI NO_2 product. *Atmos. Meas. Tech.*, *12*, 129–146. https://doi.org/10.5194/amt-12-129-2019, 2019.

Laughner, J.J. and Cohen, R.C.: Direct observation of changing NO_x lifetime in North American cities, *Science,* 366, 6466, pp. 723-727, doi: 10.1126/science.aax6832, 2019.

Levelt, P. F., van den Oord, G. H. J., Dobber, M. R., Dirksen, R. J., Malkki, A., Visser, H., de Vries, J., and Stammes, P.: The ozone monitoring instrument. *IEEE Trans. Geosci. Remote Sens.*, *44*(5), 1093–1101. https://doi.org/Urn:nbn:nl:ui:25-648485, 2006.

Levelt, P. F., Joiner, J., Tamminen, J., Veefkind, J. P., Bhartia, P. K., Stein Zweers, D. C., Duncan, B. N., Streets, D. G., Eskes, H., van der A, R., McLinden, C., Fioletov, V., Carn, S., de Laat, J., DeLand, M., Marchenko, S., McPeters, R., Ziemke, J., Fu, D., Liu, X., Pickering, K., Apituley, A., González Abad, G., Arola, A., Boersma, F., Chan Miller, C., Chance, K., de Graaf, M., Hakkarainen, J., Hassinen, S., Ialongo, I., Kleipool, Q., Krotkov, N., Li, C., Lamsal, L., Newman, P., Nowlan, C., Suleiman, R., Tilstra, L. G., Torres, O., Wang, H., and Wargan, K.: The Ozone Monitoring Instrument: overview of 14 years in space, *Atmos. Chem. Phys.*, 18, 5699–5745, https://doi.org/10.5194/acp-18-5699-2018, 2018.

Lin, J.-T., Martin, R. V., Boersma, K. F., Sneep, M., Stammes, P., Spurr, R., Wang, P., Van Roozendael, M., Clémer, K., and Irie, H.: Retrieving tropospheric nitrogen dioxide from the Ozone Monitoring Instrument: effects of aerosols, surface reflectance anisotropy, and vertical profile of nitrogen dioxide, *Atmos. Chem. Phys.*, 14, 1441–1461, https://doi.org/10.5194/acp-14-1441-2014, 2014.

Lin, J.-T., Liu, M.-Y., Xin, J.-Y., Boersma, K. F., Spurr, R., Martin, R., and Zhang, Q.: Influence of aerosols and surface reflectance on satellite NO_2 retrieval: seasonal and spatial characteristics and implications for NO_x emission constraints, *Atmos. Chem. Phys.*, 15, 11217-11241, doi:10.5194/acp-15-11217-2015, 2015.

1055   Liu, F., Duncan, B. N., Krotkov, N. A., Lamsal, L. N., Beirle, S., Griffin, D., McLinden, C. A.,
1056   Goldberg, D. L., and Lu, Z.: A methodology to constrain carbon dioxide emissions from coal-
1057   fired power plants using satellite observations of co-emitted nitrogen dioxide, *Atmos. Chem.*
1058   *Phys.*, 20, 99–116, https://doi.org/10.5194/acp-20-99-2020, 2020.

1059   Liu, M.-Y., Lin, J.-T., Boersma, K. F., Pinardi, G., Wang, Y., Chimot, J., Wagner, T., Xie, P.,
1060   Eskes, H., Van Roozendael, M., Hendrick, F., Wang, P., Wang, T., Yan, Y.-Y., Chen, L.-L.,
1061   and Ni, R.-J.: Improved aerosol correction for OMI tropospheric NO_2 retrieval over East Asia:
1062   constraint from CALIOP aerosol vertical profile, *Atmos. Meas. Tech.*, 12, 1-21,
1063   doi:10.5194/amt-12-1-2019, 2019.

1064   Lu, Z., Streets, D. G., de Foy, B., Lamsal, L. N., Duncan, B. N., and Xing, J.: Emissions of nitrogen
1065   oxides from US urban areas: Estimation from Ozone Monitoring Instrument retrievals for
1066   2005-2014, *Atmos. Chem. Phys.*, *15*(18), 10367–10383. https://doi.org/10.5194/acp-15-
1067   10367-2015, 2015.

1068   Lucht, W., Schaaf, C. B., and Strahler, A. H.: An algorithm for the retrieval of albedo from space
1069   using semiempirical BRDF models, *IEEE Trans. Geosci. Remote Sens.*, 38, 977–998, 2000.

1070   Marchenko, S., Krotkov, N. A., Lamsal, L. N., Celarier, E. A., Swartz, W. H., and Bucsela, E. J.:
1071   Revising the slant column density retrieval of nitrogen dioxide observed by the Ozone
1072   Monitoring Instrument, *J. Geophys. Res.*, 120, 5670--5692, 2015.

1073   Martin, R. V., Chance, K., Jacob., D.J., Kurosu, T.P., Spurr., R.J.D., Bucsela, E., Gleason, J.F.,
1074   Palmer, P.I., Bey, I., Fiore, A.M., Li, Q., Yantosca, R.M., Koelemeijer, R.B.A.: An improved
1075   retrieval of tropospheric nitrogen dioxide from GOME, *J. Geophys. Res.*, 107, 4437,
1076   doi:10.1029/2001JD001027, 2002.

1077   McLinden, C. A., Fioletov, V. E., Boersma, K. F., Kharol, S. K., Krotkov, N., Lamsal, L., et al.:
1078   Improved satellite retrievals of NO_2 and SO_2 over the Canadian oil sands and comparisons
1079   with surface measurements. *Atmos. Chem. Phys.*, *14*, 3637–3656.
1080   https://doi.org/10.5194/acp-14-3637-2014, 2014.

1081   Mishchenko, M. I. and Travis, L. D.: Satellite retrieval of aerosol properties over the ocean using
1082   polarization as well as intensity of reflected sunlight, *J. Geophys. Res.*, 102, 16989–
1083   17013, https://doi.org/10.1029/96JD02425, 1997.

1084   Miyazaki, K., Eskes, H., Sudo, K., Boersma, K. F., Bowman, K.,   and Kanaya, Y.: Decadal
1085   changes in global surface NO_x emissions from multi-constituent satellite data

1086   assimilation, *Atmos. Chem. Phys.*, 2, 807–837, [10.5194/acp-17-807-2017](10.5194/acp-17-807-2017), 2017.

1087 Montgomery, A., and Holloway, T.: Assessing the relationship between satellite-derived NO_2 and

1088   economic growth over the 100 most populous global cities, *J. Appl. Rem.*

1089   *Sens.*, 04, 1, [10.1117/1.jrs.12.042607](10.1117/1.jrs.12.042607), 2018.

1090 Morel, A.: Optical modeling of the upper ocean in relation to its biogeneous matter content (Case

1091   I waters), *J. Geophys. Res.,* 93, 10749–10768, https://doi.org/10.1029/JC093iC09p10749,

1092   1988.

1093 National Geophysical Data Center, 2006. 2-minute Gridded Global Relief Data (ETOPO2) v2.

1094   National Geophysical Data Center, NOAA. doi:10.7289/V5J1012Q [access

1095   date:2017/05/22].

1096 Nolin, A., Armstrong, R., and Maslanik, J.: Near real-time SSM/I EASE-grid daily global ice

1097   concentration and snow extent, Digit, Media, Natl. Snow Ice Data Center, Boulder, CO, USA,

1098   2005.

1099 Nowlan, C. R., Martin, R.V., Philip, S., Lamsal, L.N., Krotkov, N.A., Marais, E.A., Wang, S., and

1100   Zhang, Q.: Global dry deposition of nitrogen dioxide and sulfur fioxide inferred from space-

1101   based measurements, *Global Biogeochem. Cycles,* 28, 10, doi: 10.1002/2014GB004805,

1102   2014.

1103 Nowlan, C. R., Liu, X., Leitch, J. W., Chance, K., González Abad, G., Liu, C., Zoogman, P., Cole,

1104   J., Delker, T., Good, W., Murcray, F., Ruppert, L., Soo, D., Follette-Cook, M. B., Janz, S. J.,

1105   Kowalewski, M. G., Loughner, C. P., Pickering, K. E., Herman, J. R., Beaver, M. R., Long,

1106   R. W., Szykman, J. J., Judd, L. M., Kelley, P., Luke, W. T., Ren, X., and Al-Saadi, J. A.:

1107   Nitrogen dioxide observations from the Geostationary Trace gas and Aerosol Sensor

1108   Optimization (GeoTASO) airborne instrument: Retrieval algorithm and measurements during

1109   DISCOVER-AQ Texas 2013, *Atmos. Meas. Tech.*, 9, 2647–2668,

1110   https://doi.org/10.5194/amt-9-2647-2016, 2016.

1111 Palmer, P. I., Jacob, D. J., Fiore, A. M., and Martin, R. V., Air mass factor formulation for

1112   spectroscopic measurements from satellites: Application to formaldehyde retrievals from the

1113   Global Ozone Monitoring Experiment, *J. Geophys. Res.*, 106, 14539–

1114   514550, https://doi.org/10.1029/2000JD900772, 2001.

1115 Pickering, K.E., Bucsela, E., Allen, D., Ring, A., Holzworth, R., and Krotkov, N.A.: Estimates of

1116   lightning NO_x production based on OMI NO_2 observations over the Gulf of Mexico, *J.*

1117   *Geophys. Res.,* 121, 14, pp 8668-8691, DOI: 10.1002/2015JD024179, 2016.

1118 Platt, U., and Stutz, J.: Differential optical absorption spectroscopy (DOAS), principle and

1119   applications, Springer Verlag, Heidelberg, 2006.

1120 Pope, R. J., Chipperfield, M. P., Savage, N. H., Ordóñez, C., Neal, L. S., Lee, L. A., Dhomse, S.

1121   S., Richards, N. A. D., and Keslake, T. D.: Evaluation of a regional air quality model using

1122   satellite column NO_2: treatment of observation errors and model boundary conditions and

1123   emissions, *Atmos. Chem. Phys.*, 15, 5611–5626, https://doi.org/10.5194/acp-15-5611-2015,

1124   2015.

1125 Qin, W., Fasnacht, Z., Haffner, D., Vasilkov, A., Joiner, J., Krotkov, N., Fisher, B., and Spurr, R.:

1126   A geometry-dependent surface Lambertian-equivalent reflectivity product for UV–Vis

1127   retrievals – Part 1: Evaluation over land surfaces using measurements from OMI at 466 nm,

1128   *Atmos. Meas. Tech.*, 12, 3997–4017, https://doi.org/10.5194/amt-12-3997-2019, 2019.

1129 Rasool, Q. Z., Zhang, R., Lash, B., Cohan, D. S., Cooter, E. J., Bash, J. O., and Lamsal, L.

1130   N.: Enhanced representation of soil NO emissions in the Community Multiscale Air Quality

1131   (CMAQ) model version 5.0.2, *Geosci. Mod. Develop.*, 9, 3177–3197, 10.5194/gmd-9-3177-

1132   2016, 2016.

1133 Ridley, B. A. and Grahek, F. E.: A small, low flow, high sensitivity reaction vessel for NO

1134   chemiluminescence detectors, *J. Atmos. Oceanic Technol.*, 7, 307–311,

1135   https://doi.org/10.1175/1520-0426(1990)0072.0.CO, 1990.

1136 Rienecker, M. M., Suarez, M. J., Gelaro, R., Todling, R., Bacmeister, J., Liu, E., Bosilovich, M.

1137   G., Schubert, S. D., Takacs, L., Kim, G.-K., Bloom, S., Chen, J., Collins, D., Conaty, A., da

1138   Silva, A., Gu, W., Joiner, J., Koster, R. D., Lucchesi, R., Molod, A., Owens, T., Pawson, S.,

1139   Pegion, P., Redder, C. R., Reichle, R., Robertson, F. R., Ruddick, A. G., Sienkiewicz, M.,

1140   and Woollen, J.: MERRA: NASA's Modern-Era Retrospective Analysis for Research and

1141   Applications, *J. Clim.*, 24, 3624–3648, https://doi.org/10.1175/JCLI-D-11-00015.1, 2011.

1142 Rothman, L. S., Gordon., I.E., Barbe, A., Chris Benner, D., Bernath, P.F., Birk, M., Boudon, V.,

1143   Brown, L.R., Campargue, A., Champion, J.-P., Chance, K., Coudert, L.H., Dana, V., Devi,

1144   V.M., Fally, S., Flaud, J.-M., Gamache, R.R., Goldman, A., Jacquemart, D., Kleiner, I.,

1145   Lacome, N., Lafferty, W.J., Mandin, J.-Y., Massie, S.T., Mikhailenko, S.N., Miller, E.E.,

1146   Moazzen-Ahmad, N., Naumenko, O.V., Nikitin, A.V., Orphal, J., Perevalov, V.I., Perrin, A.,

1147   Predoi-Cross, A., Rinsland, C.P., Rotger, M., Šimečková, M., Smith, M.A.H., Sung, K.,

1148   Tashkun, S.A., Tennyson, J., Toth, R.A., Vandaele, A.C., Vander Auwera, J.: The HITRAN

1149   2008 molecular spectroscopic database, *J. Quant. Spectrosc. Radiat. Trans.*, 114, 533– 572,

1150   2009.

1151   Russell, A. R., Perring, A. E., Valin, L. C., Bucsela, E. J., Browne, E. C., Wooldridge, P. J., and

1152   Cohen, R. C.: A high spatial resolution retrieval of NO_2 column densities from OMI: method

1153   and evaluation, *Atmos. Chem. Phys.*, 11, 8543–8554, https://doi.org/10.5194/acp-11-8543-

1154   2011, 2011.

1155   Schaaf, C. B., Gao, F., Strahler, A. H., Lucht, W., Li, X., Tsang, T., Strugnell, N. C., Zhang, X.,

1156   Jin, Y., Muller, J.-P., Lewis, P., Barnsley, M., Hobson, P., Disney, M., Roberts, G.,

1157   Dunderdale, M., Doll, C., d'Entremont, R., Hu, B., Liang, S., and Privette, J. L.: First

1158   operational BRDF, albedo and nadir reflectance products from MODIS, *Rem. Sens. Environ.*,

1159   83, 135–148, 2002.

1160   Schaaf, C. L. B., Liu, J., Gao, F., and Strahler, A. H.: MODIS albedo and reflectance anisotropy

1161   products from Aqua and Terra, in: Land Remote Sensing and Global Environmental Change:

1162   NASA's Earth Observing System and the Science of ASTER and MODIS, Remote Sensing

1163   and Digital Image Processing Series, edited by: Ramachandran, B., Justice, C., and Abrams,

1164   M., Vol. 11, Springer-Verlag, New York, 873 pp., 2011.

1165   Schenkeveld, V. M. E., Jaross, G., Marchenko, S., Haffner, D., Kleipool, Q. L., Rozemeijer, N.

1166   C., Veefkind, J. P., and Levelt, P. F.: In-flight performance of the Ozone Monitoring

1167   Instrument, *Atmos. Meas. Tech.,* 10, 1957–1986, https://doi.org/10.5194/amt-10-1957-2017,

1168   2017.

1169   Schreier, S. F., Richter, A., Kaiser, J. W., and Burrows, J. P.: The empirical relationship between

1170   satellite-derived tropospheric NO_2 and fire radiative power and possible implications for fire

1171   emission rates of NO_x, *Atmos. Chem. Phys.*, 5, 2447–2466, 10.5194/acp-14-2447-2014, 2014.

1172   Shah, V., Jacob, D. J., Li, K., Silvern, R. F., Zhai, S., Liu, M., Lin, J., and Zhang, Q.: Effect of

1173   changing NO_x lifetime on the seasonality and long-term trends of satellite-observed

1174   tropospheric NO_2 columns over China, *Atmos. Chem. Phys. Disc.*, 1–23, 10.5194/acp-2019-

1175   670, 2019.

1176   Spurr, R. J. D.: VLIDORT: a linearized pseudo-spherical vector discrete ordinate radiative transfer

1177   code for forward model and retrieval studies in multilayer multiple scattering media, *J. Quant.*

1178   *Spectrosc. Rad. Trans.,* 102, 316–421, https://doi.org/10.1016/j.jqsrt.2006.05.005, 2006.

1179   Stammes, P., Sneep, M., de Haan, J. F., Veefkind, J. P., Wang, P., and Levelt, P. F.: Effective
1180   cloud fractions from the Ozone Monitoring Instrument: Theoretical framework and
1181   validation, *J. Geophys. Res.,* 113, D16S38, https://doi.org/10.1029/2007JD008820, 2008.

1182   Strahan, S. E., Duncan, B.N., and Hoor, P.: Observationally derived transport diagnostics for the
1183   lowermost stratosphere and their application to the GMI chemistry and transport
1184   model, *Atmos. Chem. Phys.*, **7**, 2435– 2445, 2007.

1185   Strode, S.A., Rodriguez, J.M., Logan, J.A., Cooper, O.R., Witte, J.C., Lamsal, L.N., Damon, M.,
1186   Van Aartsen, B., Steenrod, S.D., and Strahan, S.E.:Trends and variability in surface ozone
1187   over the United States, *J. Geophys. Res.*, doi: 10.1002/2014JD022784, 2015.

1188   Tang, W., Cohan, D.   S., Pour-Biazar, A., Lamsal, L.   N., White, A.
1189   T., Xiao, X., Zhou, W., Henderson, B. H., and Lash, B. F.: Influence of satellite-derived
1190   photolysis rates and NO_x emissions on Texas ozone modeling, *Atmos. Chem. Phys.*, 4, 1601–
1191   1619, 10.5194/acp-15-1601-2015, 2015.

1192   Thalman, R., and Volkamer, R.: Temperature dependent absorption cross-sections   of O_2-O_2
1193   collision pairs between 340 and 630 nm and at atmospherically relevant pressure, *Phys.*
1194   *Chem. Chem. Phys.*, 15, 15371–15381, https://doi.org/10.1039/C3CP50968K, 2013.

1195   Thornton, J. A., Wooldridge, P. J., and Cohen, R. C.: Atmospheric NO_2: in situ laser-induced
1196   fluorescence detection at parts per trillion mixing ratios, *Anal. Chem.*, 72, 528–539,
1197   https://doi.org/10.1021/ac9908905, https://doi.org/10.1021/ac9908905, 2000.

1198   Tong, D., Lamsal, L.N., Pan, L., Kim, H., Lee, P., Chai, T., Pickering, K.E.: Long-term NO_x trends
1199   over large cities in the United States during the Great Recession: Intercomparison of satellite
1200   retrievals, ground observations, and emission inventories, *Atmos. Env.,* 109, doi:
1201   10.1016/j.atmosenv.2015.01.035, 2015.

1202   Torres, O., Tanskanen, A., Veihelman, B., Ahn, C., Braak, R., Bhartia, P. K., Veefkind, V., and
1203   Levelt, P.: Aerosols and Surface UV Products from OMI Observations: An Overview, *J.*
1204   *Geophys. Res.*, 112, D24S47, https://doi.org/10.1029/2007JD008809, 2007.

1205   van der A, R. J., Eskes, H.J., Boersma, K.F., van Noije, T.P.C., Van Roozendael, M., De Smedt, I.,
1206   Peters, D. H. M. U., and Meijer E.W.: Identification of NO_2 sources and their trends from
1207   space   using   seasonal   variability   analyses, *J.   Geophys.   Res.*, 113,   D04302,
1208   doi:10.1029/2007JD009021, 2008.

1209   van Geffen, J. H. G. M., Boersma, K. F., Van Roozendael, M., Hendrick, F., Mahieu, E., De Smedt,

I., Sneep, M., and Veefkind, J. P.: Improved spectral fitting of nitrogen dioxide from OMI in the 405–465 nm window, *Atmos. Meas. Tech.*, 8, 1685–1699, https://doi.org/10.5194/amt-8-1685-2015, 2015.

Vandaele, A. C., Hermans, C., Simon, P.C., Carleer, M., Colin, R., Fally, S., Mérienne, M.F., Jenouvrier, A., and Coquart, B.: Measurements of the NO_2 absorption cross-section from 42,000 cm^{-1} to 10,000 cm^{-1} (238-1000 nm) at 220 K and 294 K, *J. Quant. Spectrosc. Radiat. Trans.*, 59, 171– 184, 1998.

Vasilkov, A., Joiner, J., Gleason, J., and Bhartia, P.K.: Ocean Raman scattering in satellite backscatter UV measurements, *Geophys. Res. Lett.*, 29, 1837, doi:10.1029/2002GL014955, 2002.

Vasilkov, A. P., Herman, J. R., Ahmad, Z., Karu, M., and Mitchell, B. G.: Assessment of the ultraviolet radiation field in ocean waters from space-based measurements and full radiative-transfer calculations, *Appl. Opt.,* 44, 2863–2869, https://doi.org/10.1364/AO.44.002863, 2005.

Vasilkov, A.P., Joiner, J., Spurr, R., Bhartia, P.K., Levelt, P., Stephens, G.: Evaluation of the OMI cloud pressures derived from rotational Raman scattering by comparisons with other satellite data and radiative transfer simulations, *J. Geophys. Res.*, 113, d15, https://doi.org/10.1029/2007JD008689, 2008.

Vasilkov, A. P., Joiner, J., Haffner, D., Bhartia, P. K., and Spurr, R. J. D.: What do satellite backscatter ultraviolet and visible spectrometers see over snow and ice? A study of clouds and ozone using the A-train, *Atmos. Meas. Tech.*, 3, 619–629, https://doi.org/10.5194/amt-3-619-2010, 2010.

Vasilkov, A., Qin, W., Krotkov, N., Lamsal, L., Spurr, R., Haffner, D., Joiner, J., Yang, E.-S., and Marchenko, S.: Accounting for the effects of surface BRDF on satellite cloud and trace-gas re- trievals: a new approach based on geometry-dependent Lambertian equivalent reflectivity applied to OMI algorithms, *Atmos. Meas. Tech.*, 10, 333–349, https://doi.org/10.5194/amt-10-333-2017, 2017.

Vasilkov, A., Yang, E.-S., Marchenko, S., Qin, W., Lamsal, L., Joiner, J., Krotkov, N., Haffner, D., Bhartia, P.K., Spurr, R.: A cloud algorithm based on the O_2-O_2 477 nm absorption band featuring an advanced spectral fitting method and the use of surface geometry-dependent Lambertian-equivalent reflectivity, *Atmos. Meas. Tech.*, 11, 4093-4107, doi: 10.5194/amt-11-

4093-2018, 2018.

Vasilkov, A., Krotkov, N., Yang, E.-S., Lamsal, L., Joiner, J., Castellanos, P., Fasnacht, Z., and Spurr, R.: Explicit and consistent aerosol correction for visible wavelength satellite cloud and nitrogen dioxide retrievals based on optical properties from a global aerosol analysis, *Atmos. Meas. Tech. Discuss.*, https://doi.org/10.5194/amt-2019-458, in review, 2020.

Veefkind J. P., de Haan, J. F., Brinksma, E. J., Kroon, M., and Levelt, P. F.: Total ozone from the Ozone Monitoring Instrument (OMI) using the DOAS technique, *IEEE Trans. Geophys. Remote Sens.*, 44, 1239–1244, 2006.

Veefkind, J. P., de Haan, J. F., Sneep, M., and Levelt, P. F.: Improvements to the OMI O_2–O_2 operational cloud algorithm and comparisons with ground-based radar–lidar observations, *Atmos. Meas. Tech.*, 9, 6035–6049, https://doi.org/10.5194/amt-9-6035-2016, 2016.

Vinken, G. C. M., Boersma, K. F., Donkelaar, A., and Zhang, L., Constraints on ship NO_x emissions in Europe using GEOS-Chem and OMI satellite NO_2 observations, *Atmos. Chem. Phys.*, 3, 1353–1369, 10.5194/acp-14-1353-2014, 2014a.

Vinken, G. C. M., Boersma, K. F., Maasakkers, J. D., Adon, M., and Martin, R. V.: Worldwide biogenic soil NO_x emissions inferred from OMI NO_2 observations, *Atmos. Chem. Phys.*, 18, 10363–10381, 10.5194/acp-14-10363-2014, 2014b.

Volkamer, R., Spietz, P., Burrows, J.P., and Platt, U., High-resolution absorption cross-section of Glyoxal in the UV/VIS and IR spectral ranges, *J. Photochem. Photobiol.*, **172**, 35– 46, doi:10.1016/j.jphotochem.2004.11.011, 2005.

Meissner, T. and Wentz, F.J.: The Complex Dielectric Constant of Pure and Sea Water from Microwave Satellite Observations. *IEEE Trans. Geo. Rem. Sens.*, 42, 1836-1849. http://dx.doi.org/10.1109/TGRS.2004.831888, 2004.

Wentz, F., Hilburn, K., and Smith, K.: RSS SSMIS ocean product grids daily from DMSP F16 NETCDF. Dataset available online from the NASA Global Hydrology Resource Center DAAC, Huntsville, Alabama, USA, https://doi.org/10.5067/MEASURES/DMSP-F16/SSMIS/DATA301, 2012.

Zara, M., Boersma, K. F., De Smedt, I., Richter, A., Peters, E., van Geffen, J. H. G. M., Beirle, S., Wagner, T., Van Roozendael, M., Marchenko, S., Lamsal, L. N., and Eskes, H. J.: Improved slant column density retrieval of nitrogen dioxide and formaldehyde for OMI and GOME-2A from QA4ECV: intercomparison, uncertainty characterisation, and trends, *Atmos. Meas.*

1272   *Tech.*, 11, 4033–4058, https://doi.org/10.5194/amt-11-4033-2018, 2018.

1273   Zhou, Y., Brunner, D., Spurr, R. J. D., Boersma, K. F., Sneep, M., Popp, C., and Buchmann, B.:

1274   Accounting for surface reflectance anisotropy in satellite retrievals of tropospheric NO_2,

1275   *Atmos. Meas. Tech.*, 3, 1185–1203, https://doi.org/10.5194/amt-3-1185-2010, 2010.

1276   Zhou, Y., Brunner, D., Hueglin, C., Henne, S., and Staehelin, J.: Changes in OMI tropospheric

1277 NO_2 columns over Europe from 2004 to 2009 and the influence of meteorological

1278   variability, *Atmos. Environ.*, 482–495, 10.1016/j.atmosenv.2011.09.024, 2012.
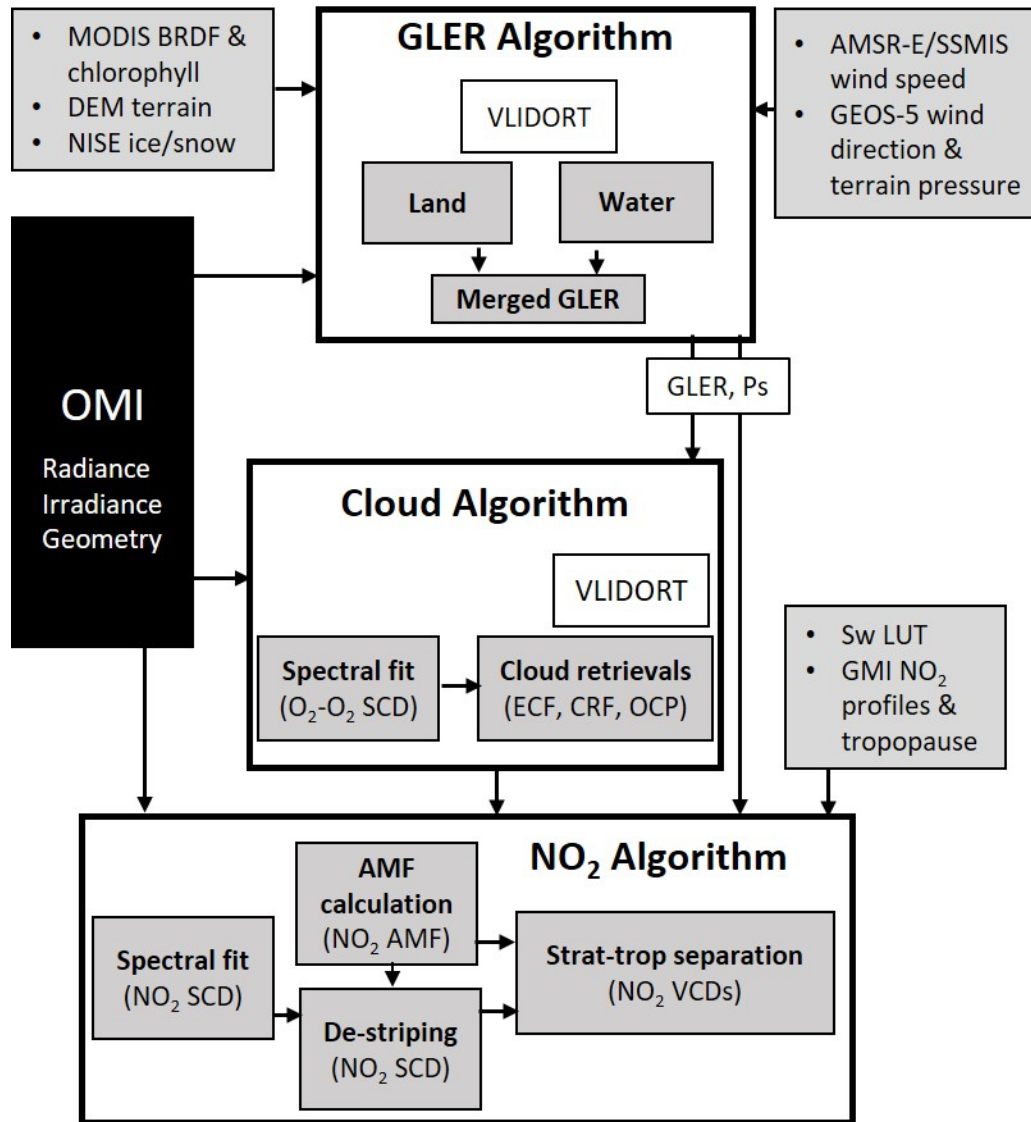
1279

Figure 1: Schematic diagram of the NASA OMI NO_2 algorithm, version 4.0, which is coupled with the cloud and geometry-dependent surface Lambertian Equivalent Reflectivity (GLER) algorithms that ultimately produces stratospheric (strat) and tropospheric (trop) NO_2 vertical column densities (VCDs). Acronyms used here are described in relevant sections below. VLIDORT: Vector Linearized Discrete Ordinate Radiative Transfer; MODIS: Moderate

1285 Resolution Imaging Spectro-radiometer; BRDF: bidirectional reflectance distribution function;
1286 DEM: Digital Elevation Model; NISE: Near-real-time Ice and Snow Extent; AMSR-E: Advanced
1287 Microwave Scanning Radiometer for Earth Observing System (EOS); SSMIS: Special Sensor
1288 Microwave Imager / Sounder; GEOS-5: Goddard Earth Observing System, Version 5; Ps: surface
1289 (terrain) pressure over OMI pixel; ECF: Effective Cloud Fraction; CRF: Cloud Radiance Fraction;
1290 OCP: Optical Centroid Pressure; Sw: Scattering weight; LUT: Look-up table GMI: Global
1291 Modeling Initiative; AMF: Air Mass Factor; SCD: Slant Column Density.
1292
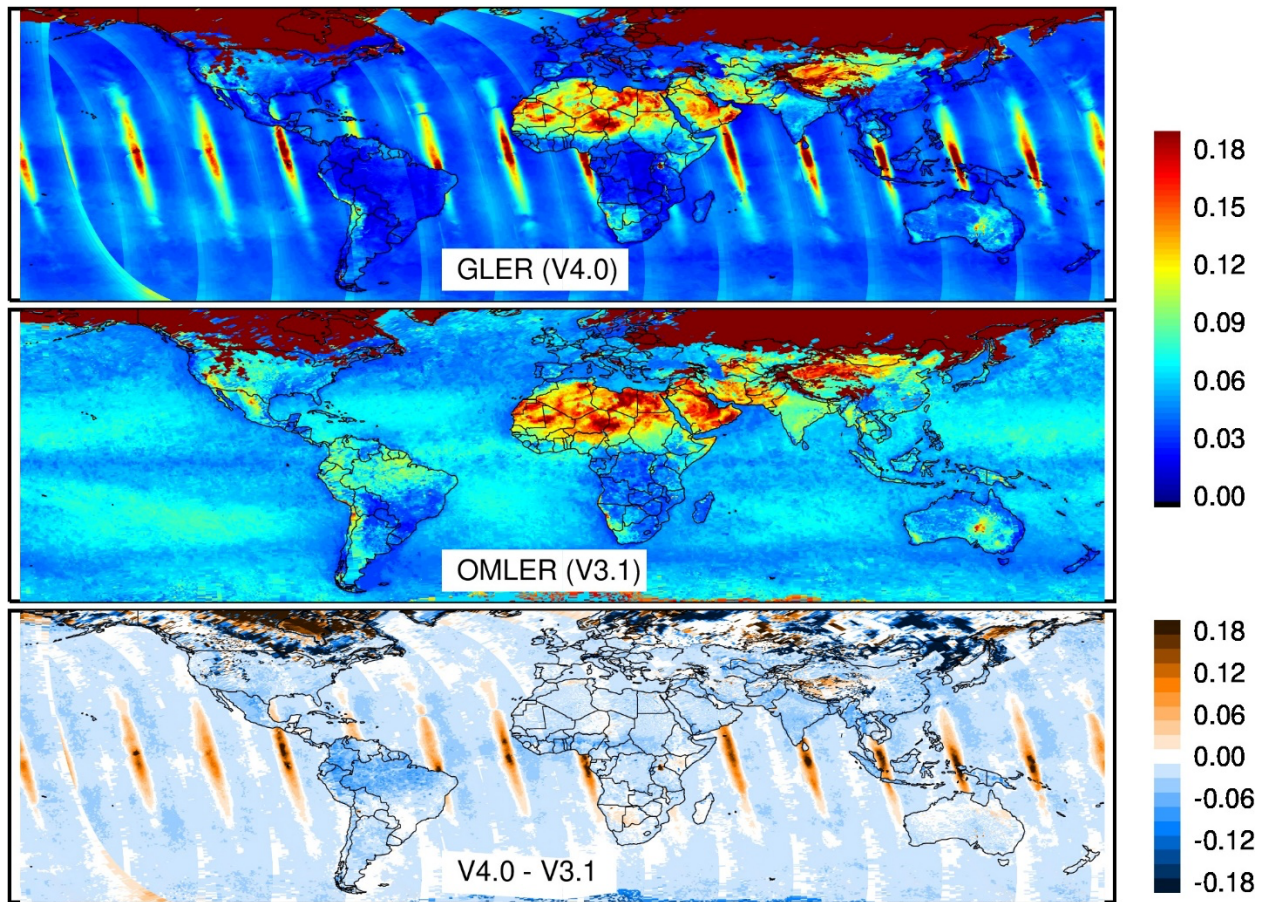
1293

1294 **Figure 2**: Surface reflectivity at 440 nm (top) derived using MODIS BRDF data with OMI
1295 geometry (GLER) on March 20, 2005 compared with (middle) OMI-based monthly LER
1296 climatology (OMLER) for the month of March (Kleipool et al., 2008). The bottom panel shows
1297 the difference between MODIS-based and climatological surface reflectivity data.
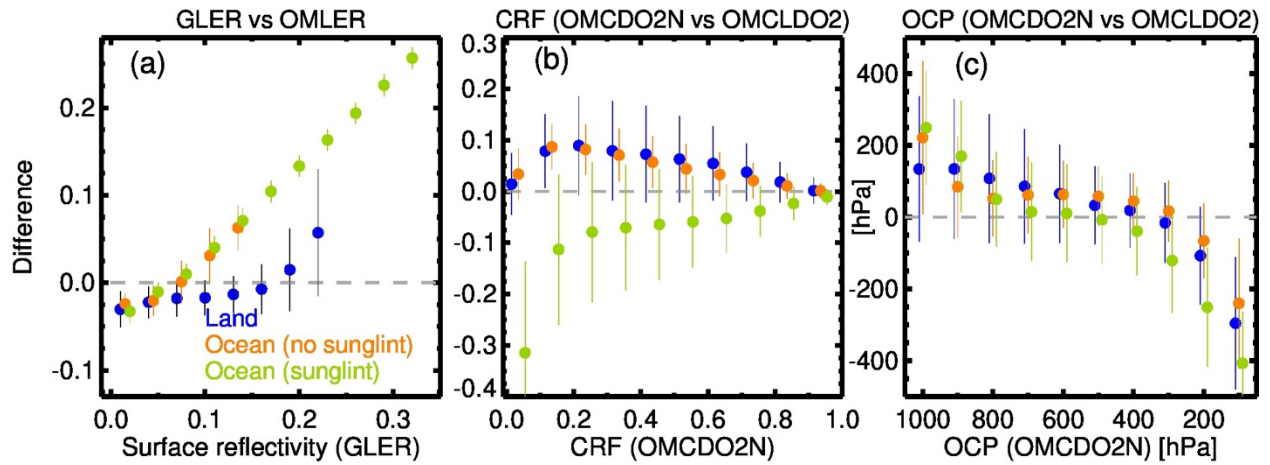
1298

1299 **Figure 3**: Differences (V4.0 – V3.1) in (a) surface reflectivity, (b) cloud radiance fraction, and (c)
1300 cloud optical centroid pressure for March 20, 2005, as used in V3.1 and V4.0 algorithms and
1301 binned by the values of corresponding parameters from V4.0. Data are separated for land (blue)
1302 and ocean surfaces, and by sunglint (green) and non-sunglint (orange) geometry over ocean. The
1303 vertical bars represent the standard deviation for each bin of those parameters.

1304
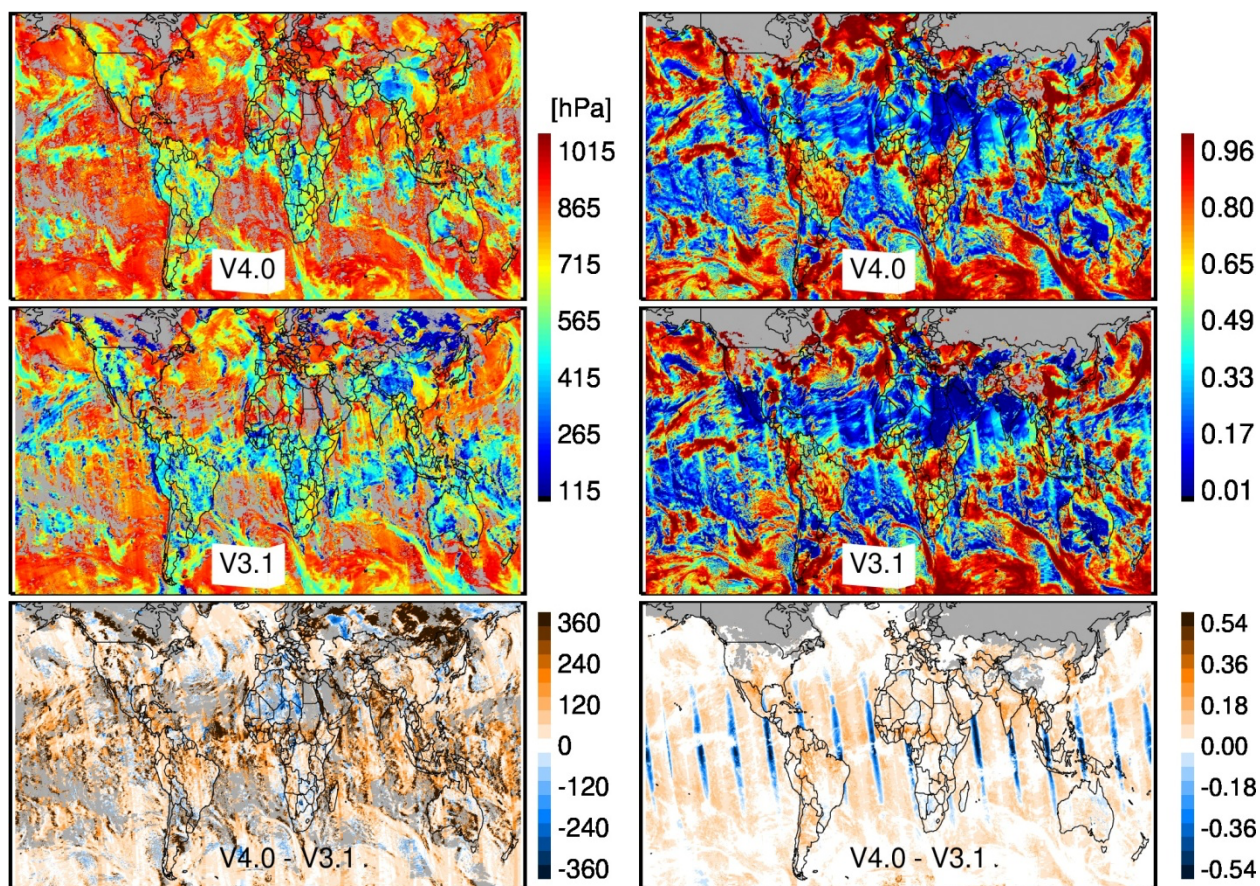
Figure 4: Cloud optical centroid pressure at 477 nm (left) and cloud radiance fraction at 440 nm (right) retrieved for March 20, 2005 with OMNO2 V4.0 (top) and V3.1 (middle) algorithms, respectively. The bottom rows show their differences. The gray color represents the OMI pixels with retrieved cloud pressure equal to terrain pressure in V4.0 on the left and over snow/ice surface identified by the NISE flag on the right.
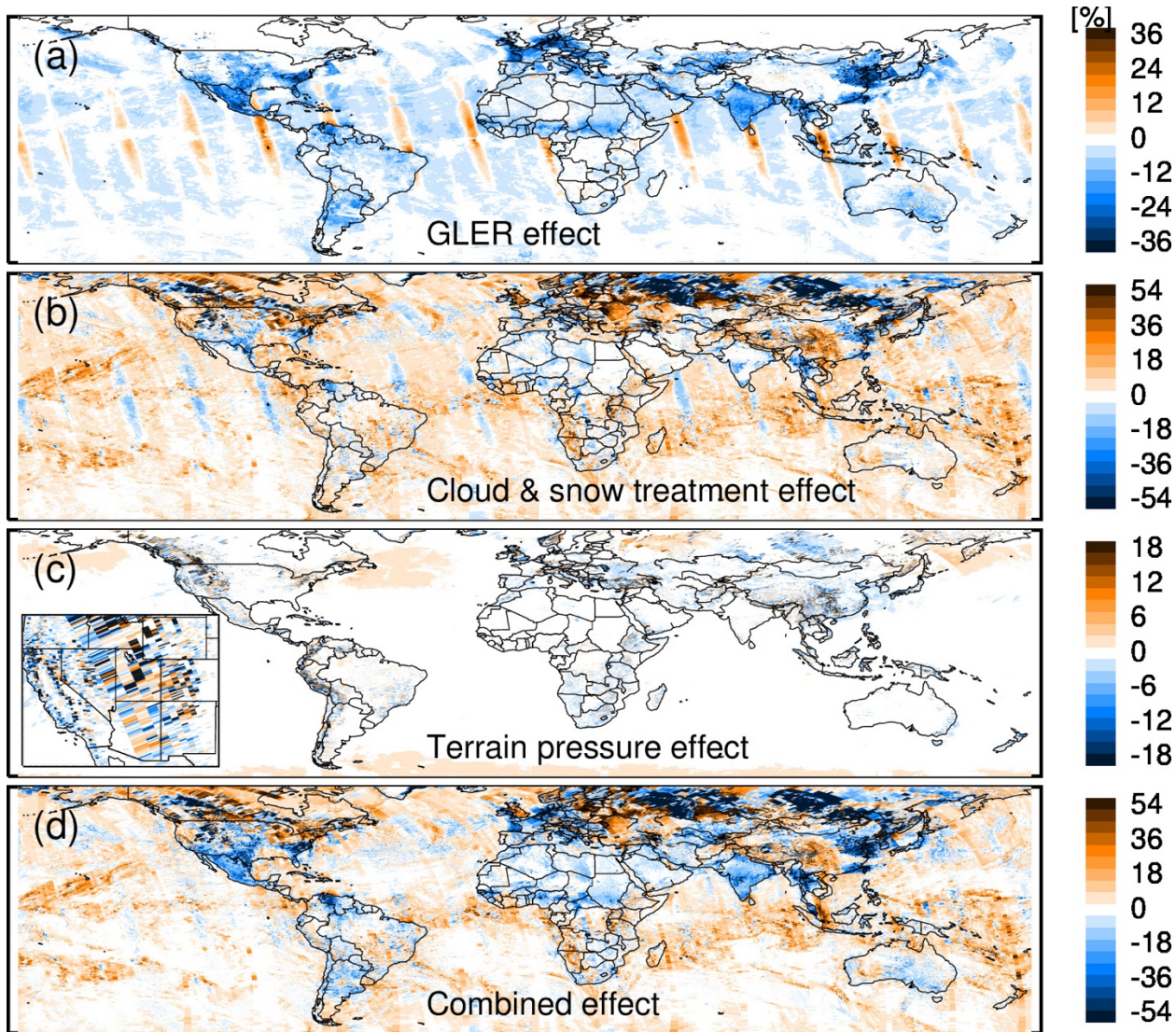
1311

1312   **Figure 5**: Impact on tropospheric AMF (i.e., V4.0 – V3.1) from changes in (a) surface reflectivity,

1313   (b) cloud and surface treatment, (c) terrain pressure, and (d) their combination on March 20, 2005.

1314   The figure 5(c) inset shows zoomed view of impact over complex terrain in the western US.
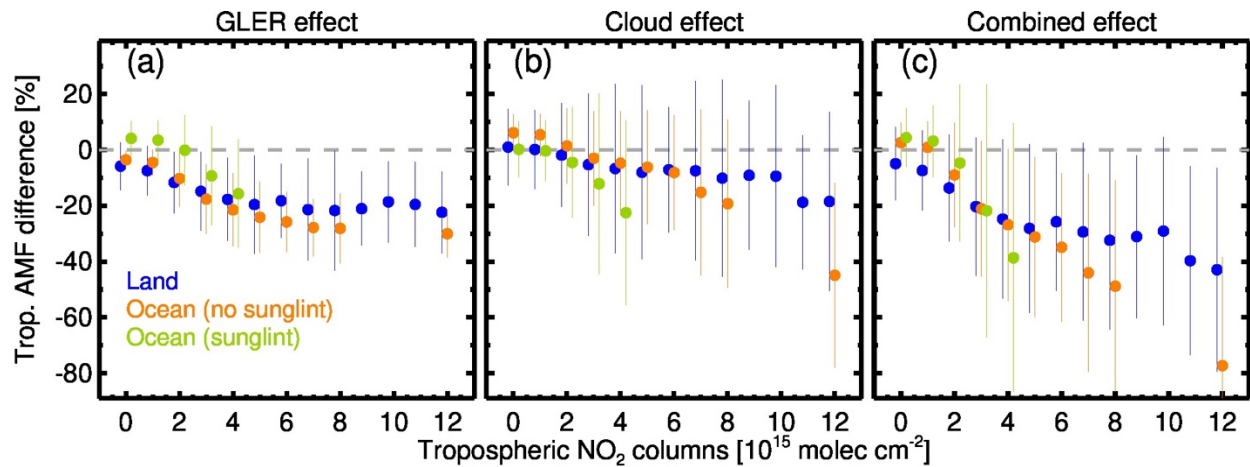
1315

Figure 6: The impact on tropospheric AMF (i.e., V4.0 – V3.1) from changes in (a) surface reflectivity, (b) cloud, and (c) their combination for clear and partially cloudy scenes (CRF<0.5) on March 20, 2005. Percent differences in tropospheric AMF are sorted by tropospheric NO_2 columns, separating them by land (blue) and ocean, and by sunglint (green) and non-sunglint (orange) geometry over ocean. The vertical bars represent the standard deviations for the tropospheric NO_2 column bins.
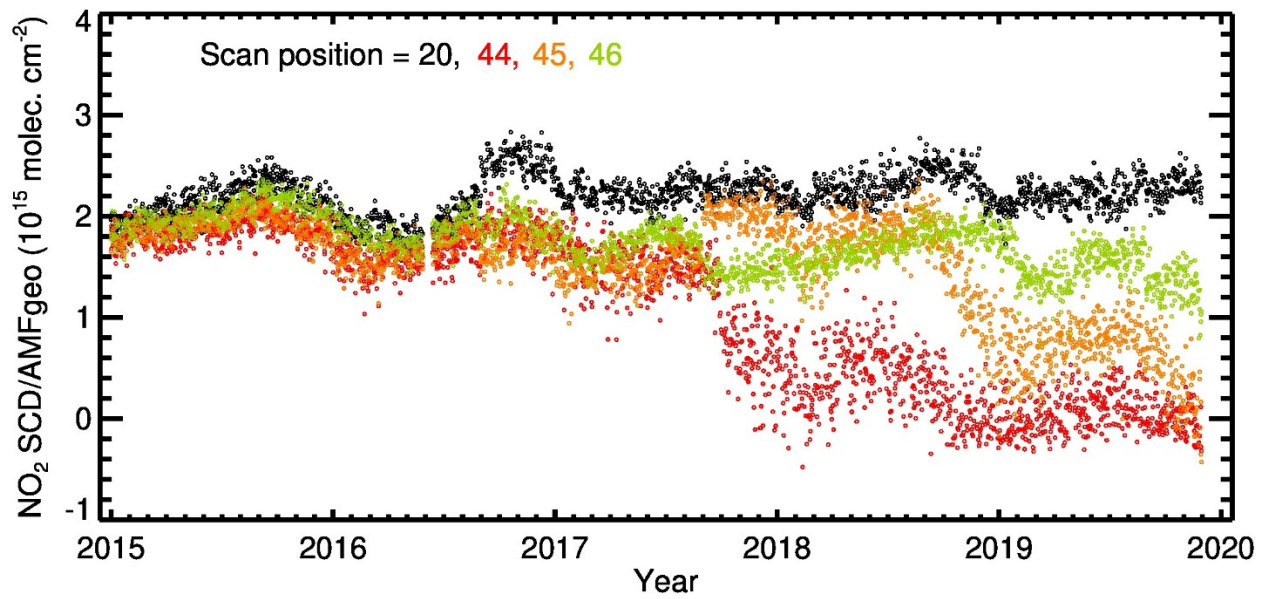
Figure 7: The time series of OMI NO$_2$ SCD normalized by the geometric AMF for clear-sky and partially cloudy conditions (CRF<0.5) over the Pacific Ocean. The data are separated by cross-track scan position, comparing the presumably RA-free row 20 (black) with rows 44 (red), 45 (orange), and 46 (green). The row numbers are 0-based.
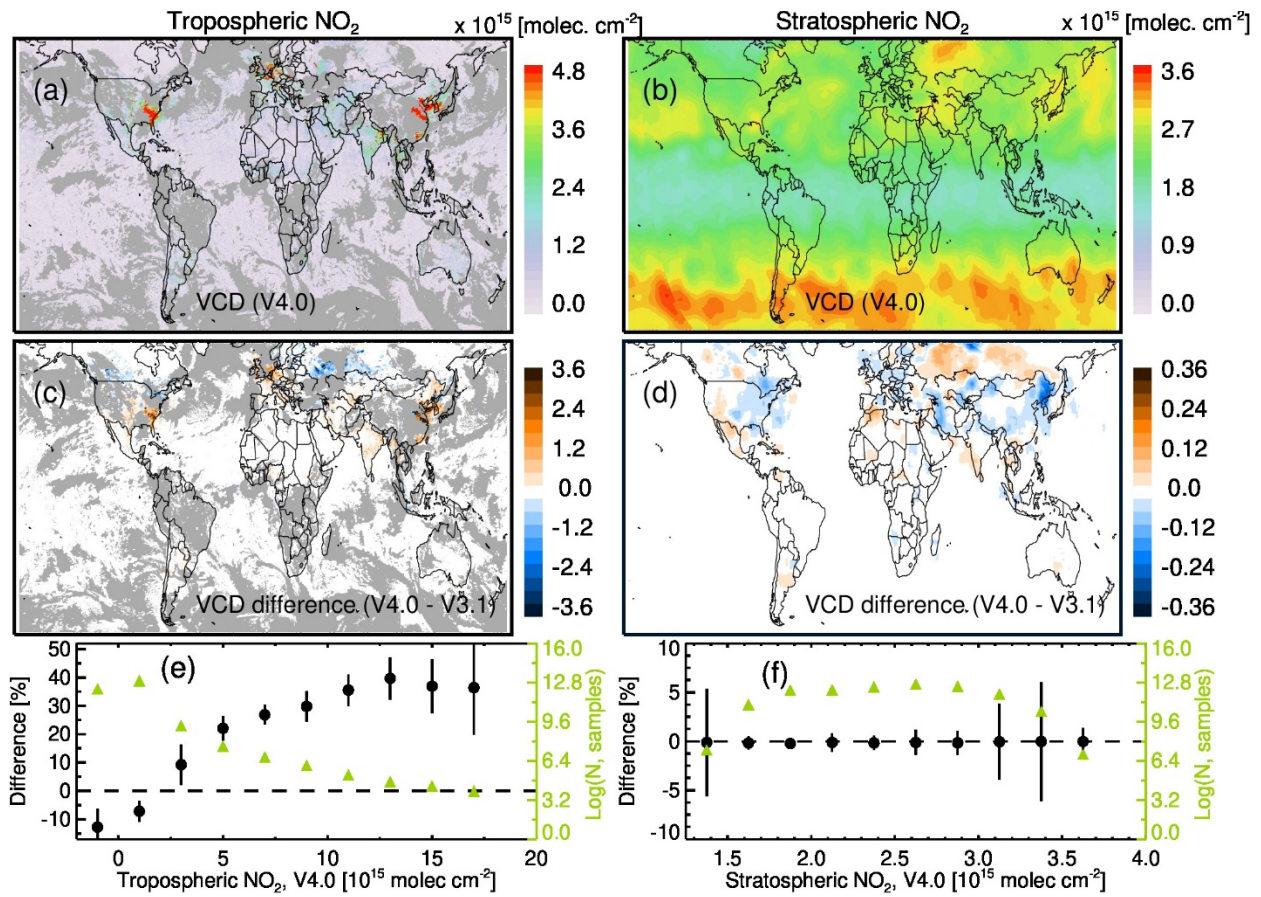
Figure 8: Tropospheric (a) and stratospheric (b) NO$_2$ VCD from V4.0 and their differences (c, d) with V3.1 data (V4.0 – V3.1) for March 20, 2005. The gray color in the tropospheric NO$_2$ maps represent cloudy areas (CRF>0.5). Bottom panels show average (black circles) and standard error (vertical bars) of the relative difference, $100 \times$ (V4.0 – V3.1)/V3.1, for tropospheric (e) and stratospheric (f) NO$_2$ VCDs plotted as a function of respective NO$_2$ column amounts. The green symbols represent the logarithm of the number of samples.
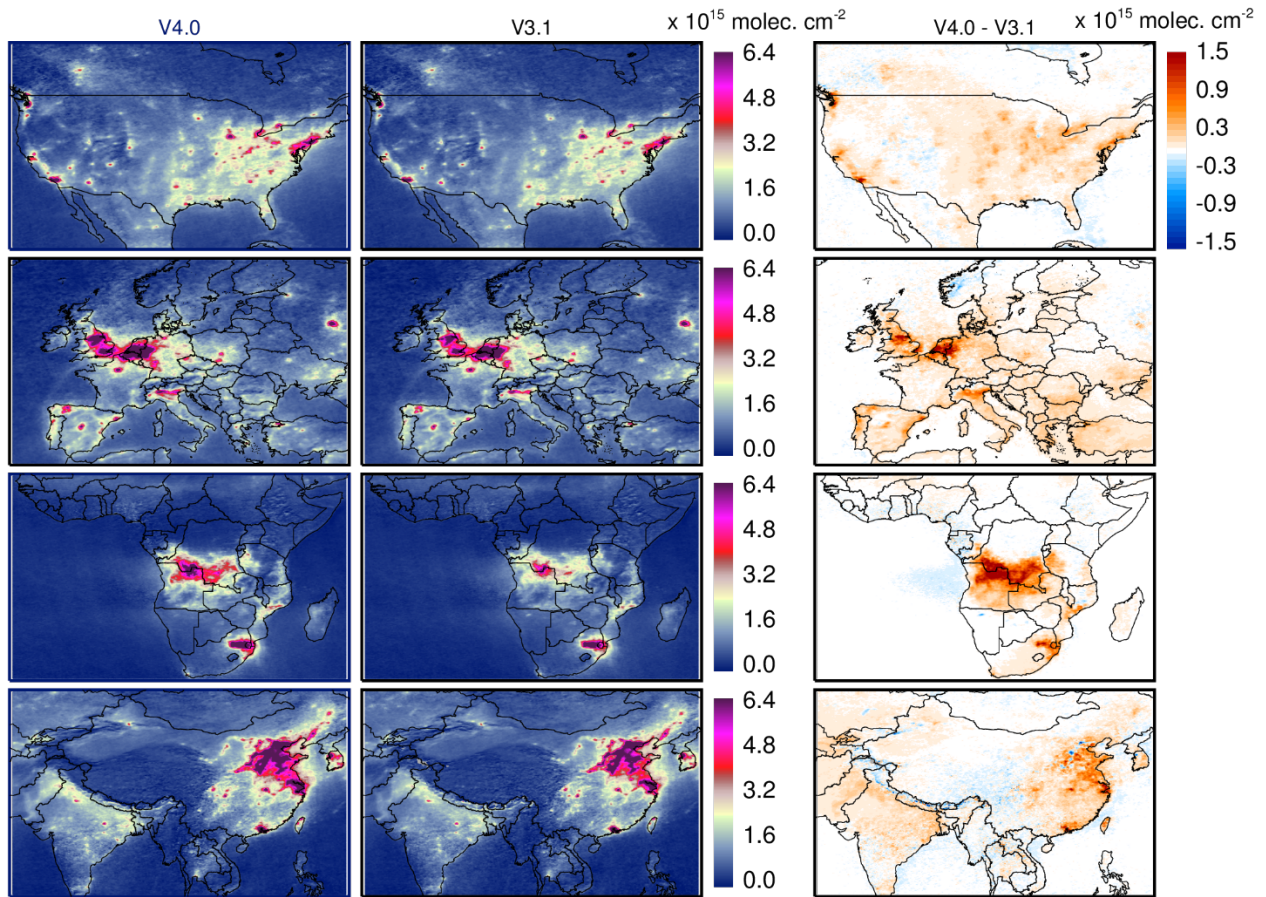
Figure 9: Three-month (June, July, August) average tropospheric NO_2 columns for low cloud conditions (CRF<0.5) in 2005 over North America (1st row), Europe (2nd row), southern Africa (3rd row), and Asia (4th row) from V4.0 (1st column), V3.1 (2nd column), and their difference (V4.0 – V3.1).
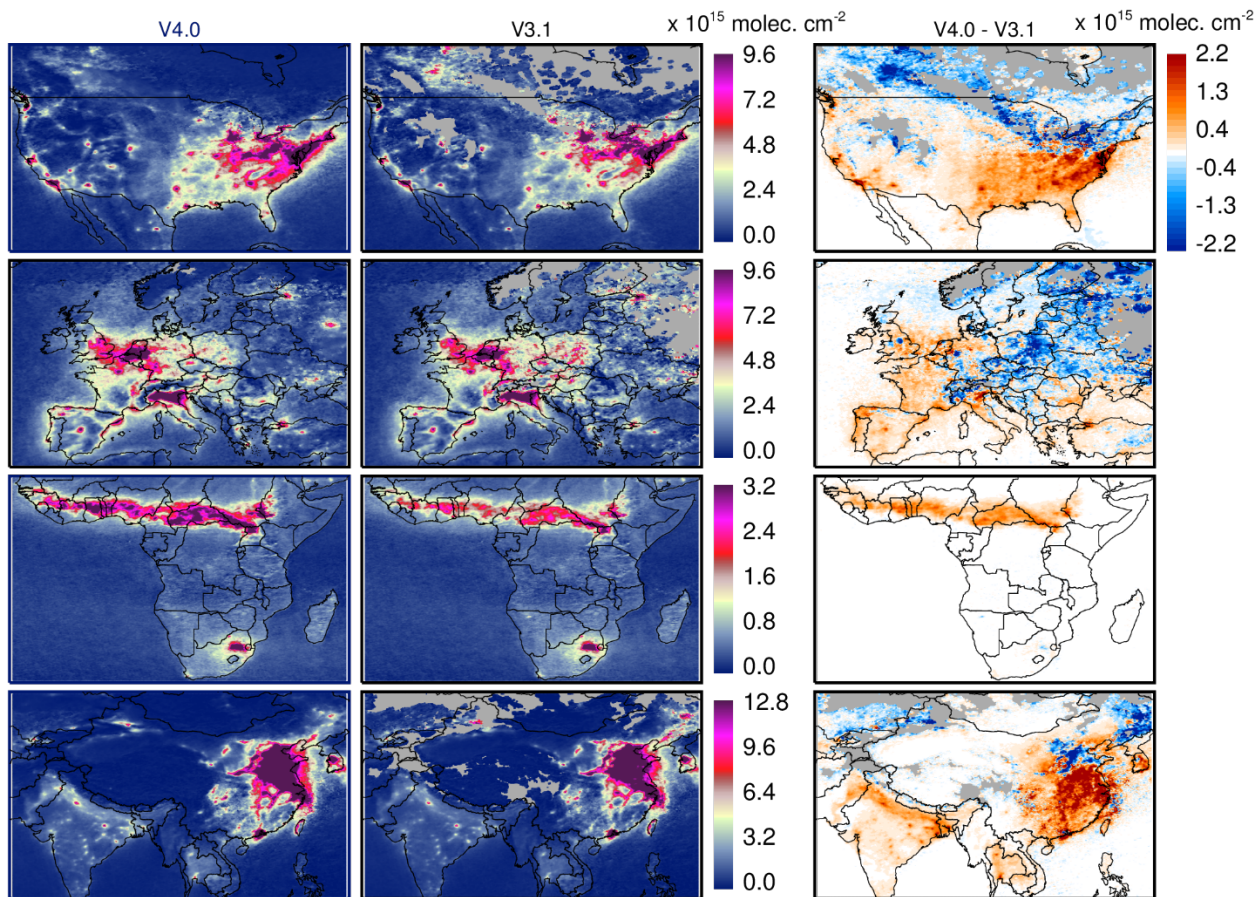
Figure 10: Same as Figure 9, but for December, January, and February. The gray areas represent a lack of good observations as determined by data quality flags.
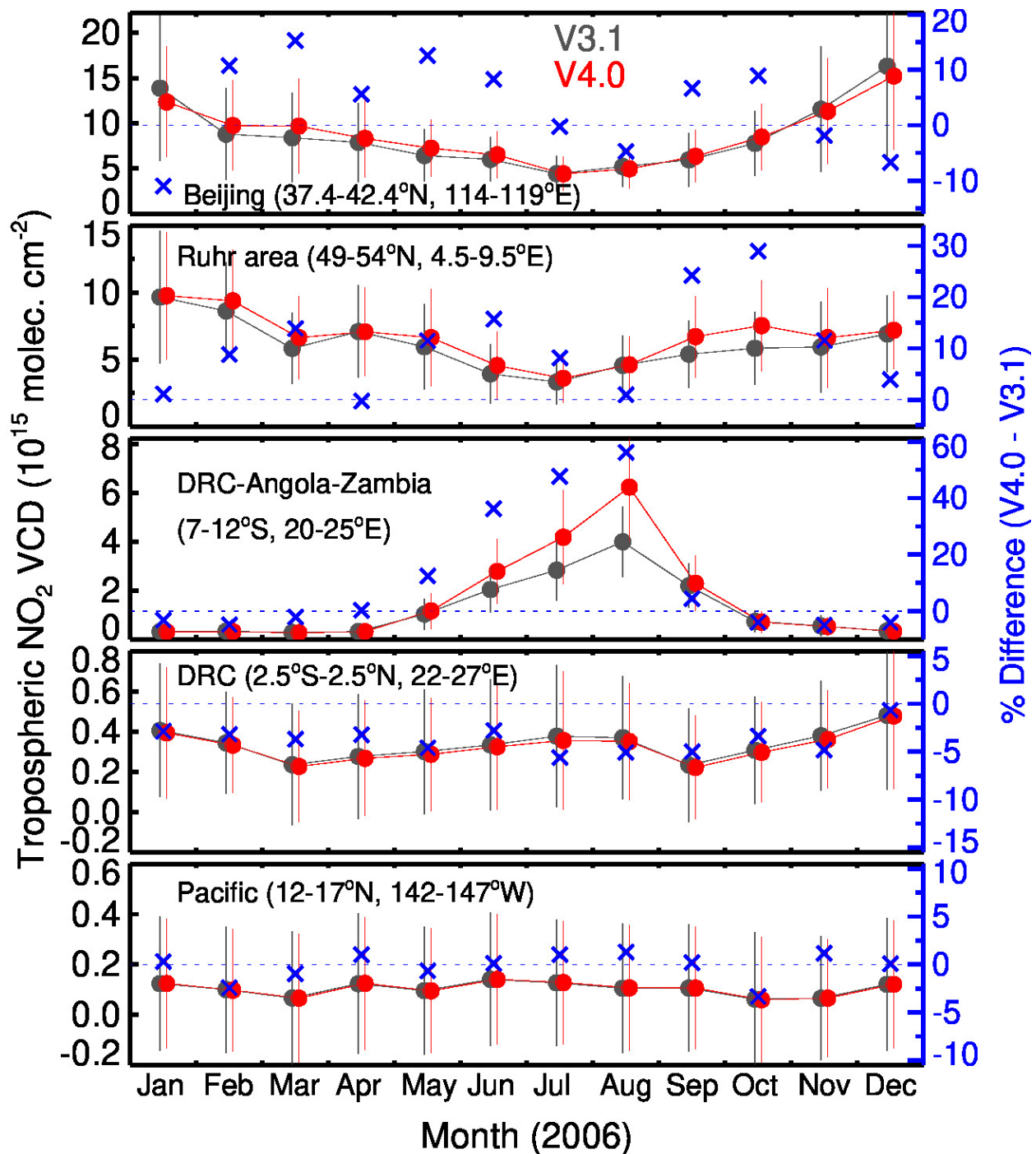
1360

1361   **Figure 11**: Monthly average tropospheric NO_2 columns in 2006 calculated from V3.1 (black)

1362   and V4.0 (red) data over selected 5º latitude × 5º longitude boxes from locations that are

1363   dominated by either anthropogenic (Beijing, China and Ruhr area, Germany), biomass burning

1364   (Democratic Republic of Congo (DRC), Angola, and Zambia), lightning (DRC), or no significant

1365   (Pacific) NO_x sources. The vertical bars show the monthly standard deviation. The blue symbols

1366 that correspond to the right y-axis show monthly relative difference (in percent) between V4.0

1367 and V3.1.
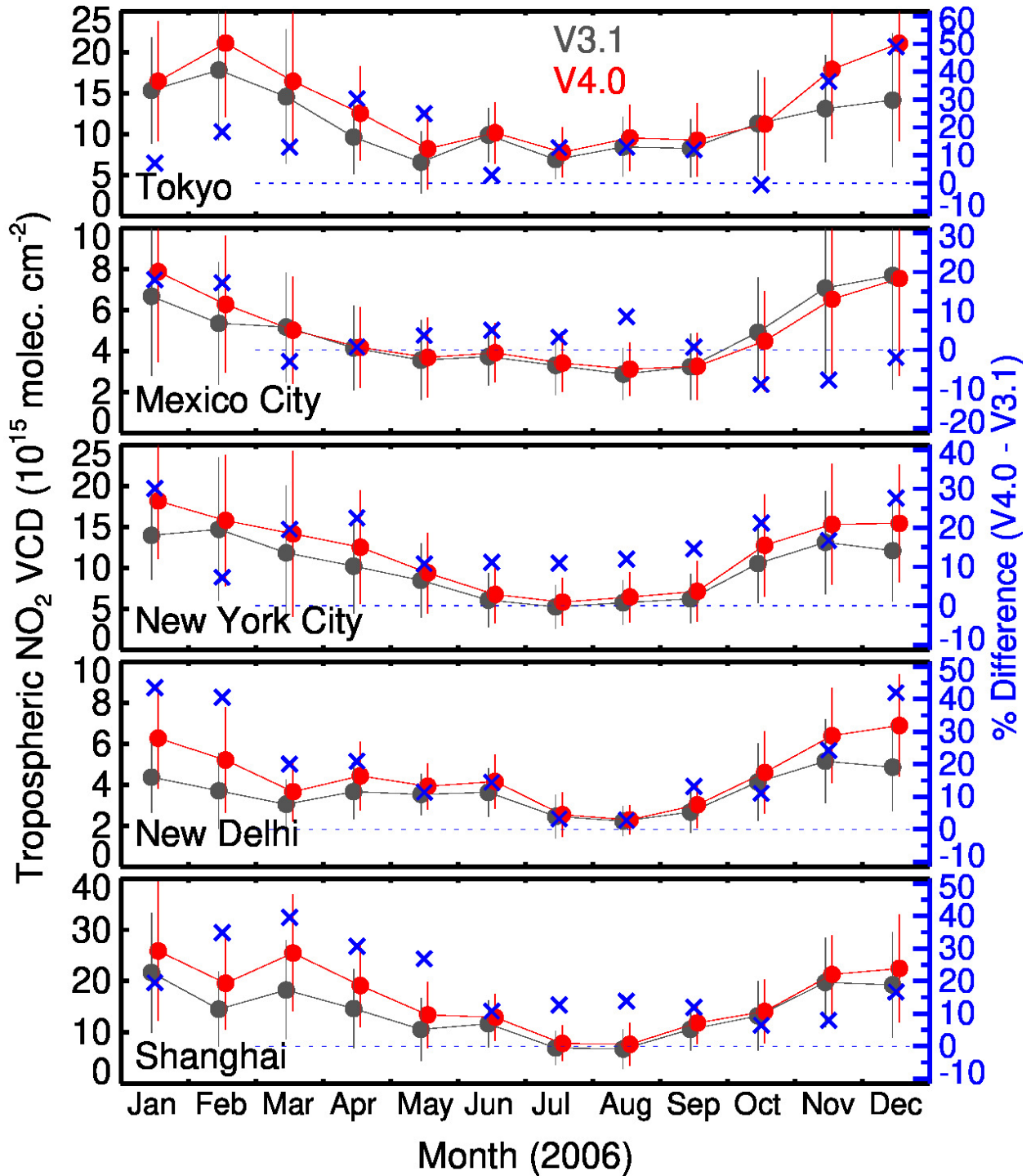
1368

1369 **Figure 12**: Same as Figure 11, but for 1º latitude × 1º longitude wide box over the five highly

1370 populated and polluted cities.

1371

1372

1373
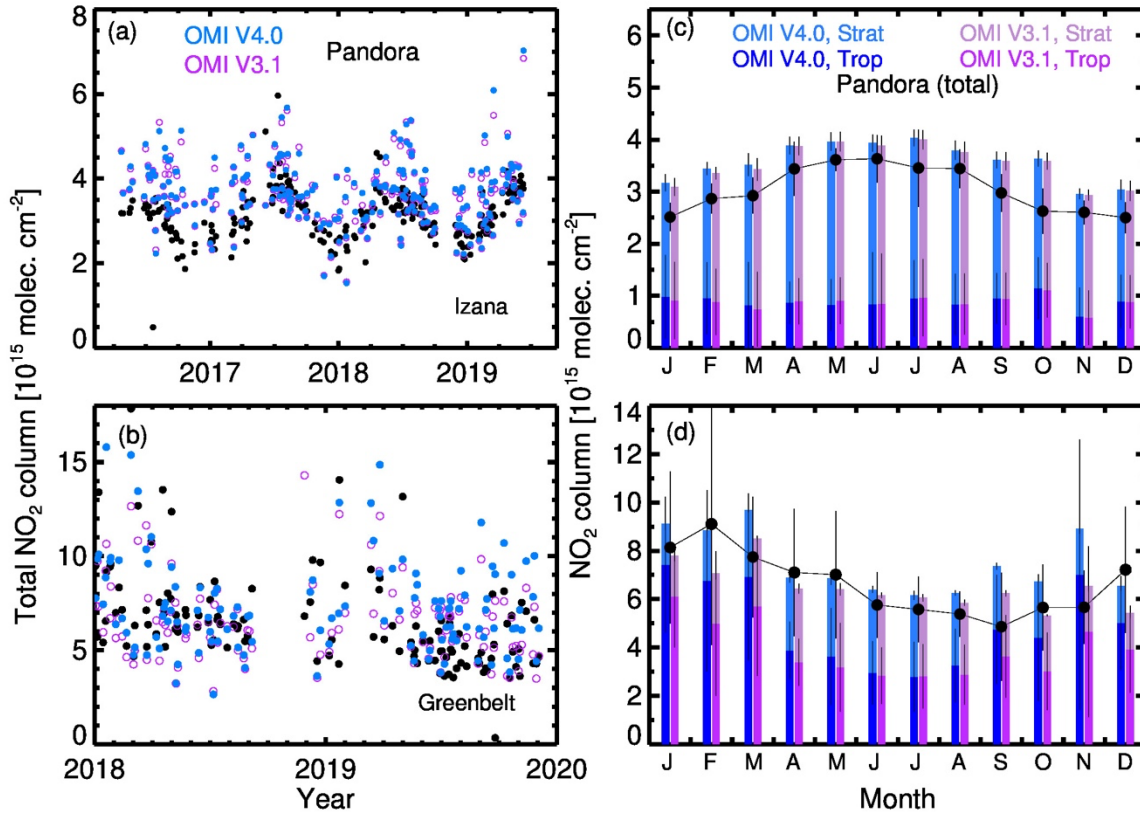
1374

Figure 13: The time series of NO₂ total columns retrieved from Pandora (black circles) and OMI
at (a) Izaña, Spain and (b) Greenbelt, Maryland, USA, with the OMI retrievals represented by the
filled blue (V4.0) and open purple (V3.1) circles. Right panels show monthly variation of NO₂
total columns at (c) Izaña for 2016–2019 and (d) Greenbelt for 2018-2019, as calculated from
Pandora (black line with filled circles) and OMI measurements (bars). OMI NO₂ total columns

1380 retrieved with V4.0 (blue) and V3.1 (purple) are separated into tropospheric and stratospheric

1381 components. The vertical lines represent the standard deviation from the average.

1382
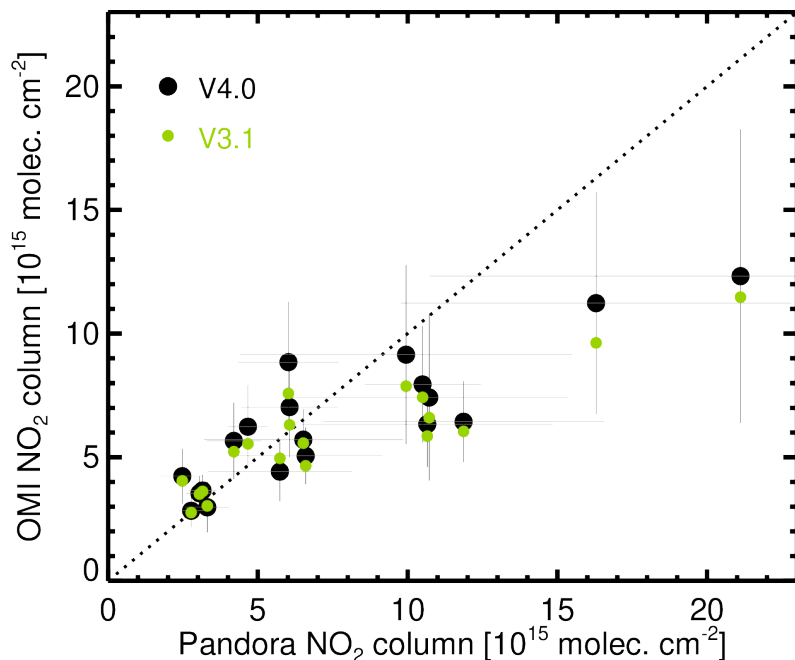
1383

1384 **Figure 14**: The scatter plot of Pandora versus OMI V4.0 (black) and V3.1 (green) average total

1385 column NO_2 for 18 Pandora sites. The vertical and horizontal lines represent the standard

1386 deviations for Pandora and OMI, respectively. The dotted line represents the 1:1 relationship.

1387
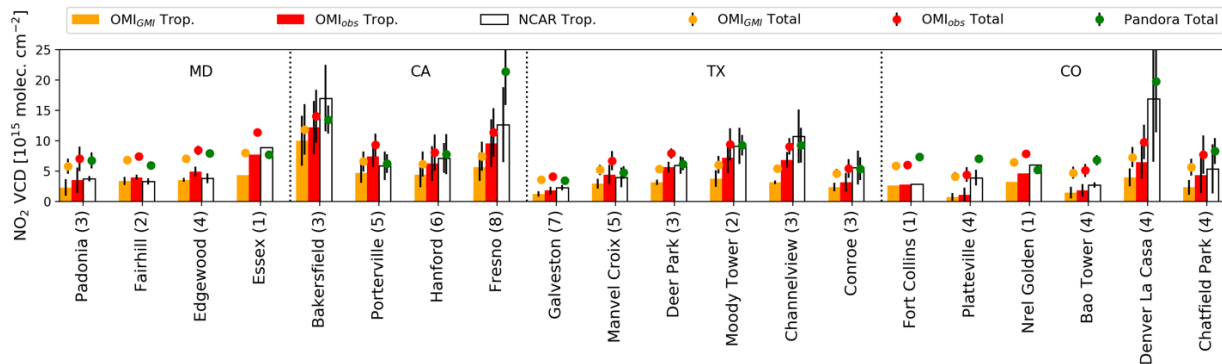
1388

1389 **Figure 15**: Site average total (circles) and tropospheric (bars) NO_2 column data from P-3B spiral

1390 (white bars), Pandora (green circles), and OMI (orange and red). The OMI tropospheric columns

1391   are derived using GMI-simulated (OMI_{GMI}, orange) and P-3B (OMI_{obs}, red) NO_2 profiles. The

1392   vertical bars for sites with over 2 observations represent the standard deviations.

1393

1394   **Table 1**. Summary of algorithms and approaches used in the NASA NO_2 algorithms versions 3.1 and 4.0

Algorithm Component		Version 3.1 (Released 2018)	Version 4.0 (Released 2019)
Spectral fit	NO_2	Modified DOAS fit (Marchenko et al, 2015)	Same as in V3.1
	O_2-O_2	DOAS fit from KNMI (Veefkind et al, 2016)	Modified DOAS fit (Vasilkov et al, 2018)
AMF	Terrain reflectivity	Monthly climatology (Kleipool et al., 2008)	Daily GLER data (Vasilkov et al., 2017; Qin et al., 2019; Fasnacht et al., 2019)
	Terrain pressure	At pixel center (calculated from terrain height and GMI terrain pressure)	Average over pixel (calculated from terrain height and GMI terrain pressure)
	Cloud pressure and fraction	Operational O_2-O_2 cloud product (OMCLDO2) v2.0 (Veefkind et al., 2016)	New O_2-O_2 cloud product (OMCDO2N) derived using the GLER product (Vasilkov et al., 2018)
	Cloud radiance fraction	Calculated at 440 nm from OMCLDO2 v2.0 cloud fraction using VLIDORT-based look-up-table	Calculated at 440 nm from OMCDO2N cloud fraction using VLIDORT-based look-up-table
	Scattering weights	TOMRAD-based look-up table	Same as in V3.1
	A-priori NO_2 profiles	GMI-derived yearly varying monthly mean profiles at 1°×1.25°	Same as in V3.1
Stripe correction		Based on data from 30°S - 5°N of 5 orbits	Same as in V3.1
Stratosphere-troposphere separation		Spatial filtering and interpolation (Bucsela et al., 2013), but with minor changes in box sizes	Same as in V3.1

1395

1396

1397

1398

1399

1400   **Table 2:** Comparison of OMI NO_2 retrievals based on a priori NO_2 profiles from GMI (OMI V4.0)

1401   and P-3B aircraft observations (OMI$_{obs}$) with P-3B and Pandora column observations during the

1402   DISCOVER-AQ field campaign. Shown here are correlation coefficient (r) and mean difference,

1403   which is calculated as OMI minus validation data.

Campaign locations	OMI V4.0 vs P-3B		OMI$_{obs}$ vs P-3B		OMI (V4.0) vs Pandora		OMI$_{obs}$ vs Pandora	
	Mean diff. (%)	r	Mean diff. (%)	r	Mean diff. (%)	r	Mean diff. (%)	r
Maryland	-33.9	0.40	-5.0	0.69	-13.0	0.13	25.6	0.27
California	-44.6	0.81	-18.7	0.83	-49.8	0.33	-24.6	0.49
Texas	-53.7	0.68	-18.8	0.85	-25.3	0.67	31.7	0.81
Colorado	-66.2	0.70	-45.4	0.70	-67.6	0.70	-46.7	0.65
All	-50.3	0.74	-23.1	0.79	-46.9	0.56	-16.3	0.63

1404

1405